doi:10.26443/seismica.v5i2.1411

SEISMICA

Validation framework for semi-stochastic simulations in Cascadia earthquake early warning

Tara A. Nye * † [1], **Valerie J. Sahakian** [1], **Angela Schlesinger** [2], **Diego Melgar** [1], **Alireza Babaie Mahani** ‡ [2], **Amy Williamson** [3], **Eli Ferguson** [2], **Angela Lux** [3], **Benoît Pirenne** [2]

[1]Department of Earth Sciences, University of Oregon, Eugene, Oregon, USA, [2]Ocean Networks Canada, University of Victoria, Victoria, British Columbia, Canada, [3]Berkeley Seismology Lab, University of California Berkeley, Berkeley, California, USA

Author contributions: *Conceptualization*: Valerie J. Sahakian, Angela Schlesinger. *Data Curation*: Tara A. Nye, Angela Schlesinger, Alireza Babaie Mahani, Amy Williamson, Eli Ferguson, Angela Lux. *Formal Analysis*: Tara A. Nye, Valerie. J. Sahakian, Diego Melgar. *Funding acquisition*: Benoît Pirenne, Valerie J. Sahakian. *Investigation*: Tara A. Nye, Angela Schlesinger, Alireza Babaie Mahani, Amy Williamson, Eli Ferguson. *Methodology*: Tara A. Nye, Valerie J. Sahakian, Angela Schlesinger. *Project Administration*: Valerie J. Sahakian, A. Schlesinger. *Resources*: Angela Schlesinger. *Software*: Tara A. Nye, Angela Schlesinger, Diego Melgar, Alireza Babaie Mahani, Amy Williamson, Eli Ferguson. *Supervision*: Valerie J. Sahakian, Angela Schlesinger. *Validation*: Tara A. Nye. *Visualization*: Tara A. Nye, Angela Schlesinger, Amy Williamson. *Writing - Original draft*: Tara A. Nye. *Writing - Review & Editing*: Tara A. Nye, Valerie J. Sahakian, Angela Schlesinger, Diego Melgar, Alireza Babaie Mahani, Amy Williamson, Angela Lux.

Abstract We generate a synthetic earthquake dataset for the Cascadia region and present a framework for validating simulations for use in testing earthquake early warning (EEW) performance. The Cascadia Subduction Zone (CSZ) offshore western North America has hosted ∼**M**9 earthquakes (the most recent being in 1700 C.E.), but few moderate-to-large earthquakes have been recorded here on seismic instruments. Synthetic seismic and geodetic data provide a useful supplement to the paucity of recorded data necessary for testing EEW; however, no published study to date has validated simulations and their output for such applications. We use a set of 1D semi-stochastic forward modeling codes to generate 112 **M**6.6–9.4 CSZ rupture scenarios and waveforms for 191 sites between Oregon and British Columbia. We validate the waveforms based on features critical to EEW infrastructure, which include event detection success, magnitude estimation, and ground-motion intensities. We also present an example performance test of the ShakeAlert EPIC and Ocean Networks Canada early warning algorithms using six of the simulated events. Through the validation process, we find the simulated data represent real earthquakes scenarios well and to be a valuable component in the training of EEW algorithms for the Cascadia region.

Production Editor:
Gareth Funning
Handling Editor:
Christie Rowe
Copy & Layout Editor:
Nathalie Redick

Signed reviewer(s):
Martin van den Ende

Received:
12 July 2024
Accepted:
3 June 2026
Published:
3 August 2026

Non-technical summary Earthquake early warning systems (EEW) aim to detect earthquakes and issue alerts before strong shaking is felt. These EEW systems are often trained and tested using previously recorded earthquakes to improve accuracy and timeliness of the alerts. The Cascadia Subduction Zone (CSZ) offshore western North America hosts periodic major earthquakes, but few earthquakes are recorded on a regular basis. In other words, we lack real earthquake records for testing EEW in the Cascadia region. As an alternative, simulated earthquake data can be used as a test dataset. We generate simulated CSZ earthquake slip patterns and waveforms of felt shaking, which we validate to ensure they resemble real earthquakes regarding characteristics that influence EEW alerts. We also test six of the events with existing EEW systems in the Cascadia region. The simulated data are found to represent real earthquakes well, suggesting value in their use for training EEW algorithms.

1 Introduction

Earthquake early warning (EEW) has been at the forefront of seismological research for several decades. The concept of a real-time alert system was initially proposed in the late 1800s by J.D. Cooper (Cooper, 1868), and advancements in seismic instrumentation and telecommunication prompted implementation of local EEW systems for specific users in Japan in the 1960s–1970s (Allen, 2011), with the first public roll out of an EEW system in Mexico in 1991 (Suárez et al., 2018). As of today, public EEW systems are currently active or under development in the United States (McGuire et al., 2025), Central America (Massin et al., 2026), Canada (Crane et al., 2023; Schlesinger et al., 2021), Japan (Nakamura, 1988), South Korea (Sheen et al., 2017), Taiwan (Wu et al., 2021), China (Zhang et al., 2016), India (Chamoli et al., 2021), Italy (Zollo et al., 2009), and Eastern Europe (Clinton et al., 2016). Although varying in technical details, the first alert issued by most EEW systems is from information recorded in the initial P-waves, which are not strong enough to cause damaging shaking. This can be leveraged to forecast future shaking and provide seconds to minutes of warning time to the public and special groups of interest. Ideally, these alerts provide enough time for individuals to take cover and for critical operations to be protected, such as

*Corresponding author: tara.nye@aecom.com
†Now at AECOM, Oakland, California, USA
‡Now at BGC Inc., Vancouver, British Columbia, Canada

electric isolation of computer systems and power grids, shutting down of nuclear power plants and rail systems, and protection of hospitals and fire stations (Allen and Melgar, 2019).

Testing and validating EEW systems performance is critical because the algorithms are fully automated and have no human interaction at any point in the processing chain, and because the consequences of missed or false alerts are significant. Time-series data from real regional earthquakes are often used in offline validation tests because they capture the unique crustal properties inherent to the region and are likely representative of future ground motions. However, there are instances where observed data may be insufficient, such as in regions with high seismic potential but less frequent seismicity (e.g., Central, Eastern, and Northwestern United States), or in other regions experiencing high seismicity, yet lacking seismic or geodetic instrumentation (e.g., central and Southeast Asia, Eastern Africa, and some small island nations). On a global scale, there is a need to build systems capable of alerting large **M**8.5+ (moment magnitude) events, which contribute significantly to seismic hazard, but near-field data are minimal due to their long recurrence intervals of several centuries. For such circumstances, simulated earthquake scenarios are a valuable supplement (e.g., Lin et al., 2021; Ruhl et al., 2017; Thompson et al., 2023; Zollo et al., 2009).

Earthquake simulations have been used in a variety of applications, including investigating effects of Earth structure on rupture kinematics (e.g., Rodgers et al., 2019; Harris et al., 2021), improving seismic hazard assessments (e.g., Aagaard et al., 2001; Graves et al., 2011; Melgar, 2026; Poulos et al., 2026), and training EEW systems (Lin et al., 2021). However, validation of the models used to generate the data have focused primarily on rupture physics, and to some extent ground motions (e.g., Lin et al., 2021; Melgar et al., 2016; Small and Melgar, 2023). A validation framework has not yet been published for the generation of simulated data for use as a training mechanism for EEW, especially for shaking-related intensity measures in the Cascadia region. In this study, we (1) generate a comprehensive dataset of kinematic slip models and associated waveforms for use in testing EEW, (2) evaluate these data based on the key components of EEW systems (i.e., earthquake detection, magnitude estimation, and ground-motion intensity) using the CSZ as a case study, and (3) run a subset of the simulations through offline tests using the ShakeAlert EPIC and Ocean Networks Canada early warning algorithms.

2 Cascadia Region EEW

The CSZ is the tectonic boundary between the North American Plate and the Explorer, Juan de Fuca, and Gorda plates, extending 1,100 km from northern California to southwestern British Columbia (Figure 1). Historically, the CSZ has hosted large **M**8–9 earthquakes, with the last major rupture occurring in 1700 C.E. (Satake et al., 2003; Walton et al., 2021; Wirth et al., 2022). Although the CSZ is capable of generating large earthquakes, it experiences very little background seismicity other than intraslab earthquakes and a few patches along the megathrust offshore central Oregon (Bostock et al., 2019; Tréhu et al., 2015; Wang and Tréhu, 2016). To date, no **M**6+ CSZ interface events have been recorded on modern instruments. Due to its limited seismicity, the seismic potential of the CSZ was not realized until the late 1980s (Atwater, 1987). Such earthquake quiescence poses a challenge for assessment and mitigation of seismic hazard since building, transportation, and communication infrastructures were not designed to withstand shaking from a large earthquake (Butler, 2018; Cutts et al., 2017).

Since the 1700 event, the CSZ has accumulated significant strain. Some paleoseismic studies have estimated the probability of a full margin ($\sim$**M**9) rupture by 2062 to be 7–12% (Goldfinger et al., 2012). Most of the population in the Cascadia region lives within 300 km of the trench and could experience shaking equal to modified Mercalli intensity (MMI) $\geq$ VII during an **M**9 event (Madin and Burns, 2013; Wirth et al., 2020). The likelihood of a large ($\sim$**M**8) partial margin rupture initiating along the southern margin is around 37–42% (Goldfinger et al., 2012). Such an event could still generate moderate-to-strong shaking (i.e., MMI V–VI) along the central Oregon coast and potentially as far north as the central Washington coast (Priest et al., 2014).

EEW will be critical for reducing impact when the next large earthquake occurs, and EEW systems are especially advantageous in the Cascadia region because they can provide more warning time than in a continental strike-slip setting due to the greater distance from the fault to population centers. Evaluating EEW performance is challenging for a major CSZ rupture, not only because of the dearth of data to test such algorithms, but also because the megathrust extends along two countries (Canada and the U.S.). Hence, different EEW algorithms, seismic networks, detection boundaries, and alerting policies are in place.

ShakeAlert is the U.S. EEW system, which expanded coverage from California to Oregon and Washington in 2020 (Kohler et al., 2020). The current version of ShakeAlert (V3; McGuire et al., 2025) is supported by three source characterization algorithms: EPIC, FinDer, and GFAST-PGD. EPIC is a modified version of the ElarmS-3 point source algorithm (Chung et al., 2019; Kohler et al., 2017), which uses a short-term average/long-term average (STA/LTA) trigger for event detection. Once an event is detected, the earthquake magnitude and hypocenter location are estimated through source characterization algorithms using the first few seconds of the P-wave amplitude. FinDer is a finite fault algorithm, which uses evolving peak ground accelerations (PGA) to estimate the line source and characterize the rupture for moderate-to-large events (Allen and Melgar, 2019; Böse et al., 2018, 2023). It is usually slower than EPIC by 0.1–3.5 s for initial detections but provides more accurate magnitude estimates and is used to update alerts as the rupture progresses (Böse et al., 2022). GFAST-PGD is the newest algorithm and uses geodetic peak ground displacement (PGD) from Global Navigation Satellite System (GNSS) data to estimate event magnitudes for large earthquakes given a lo-

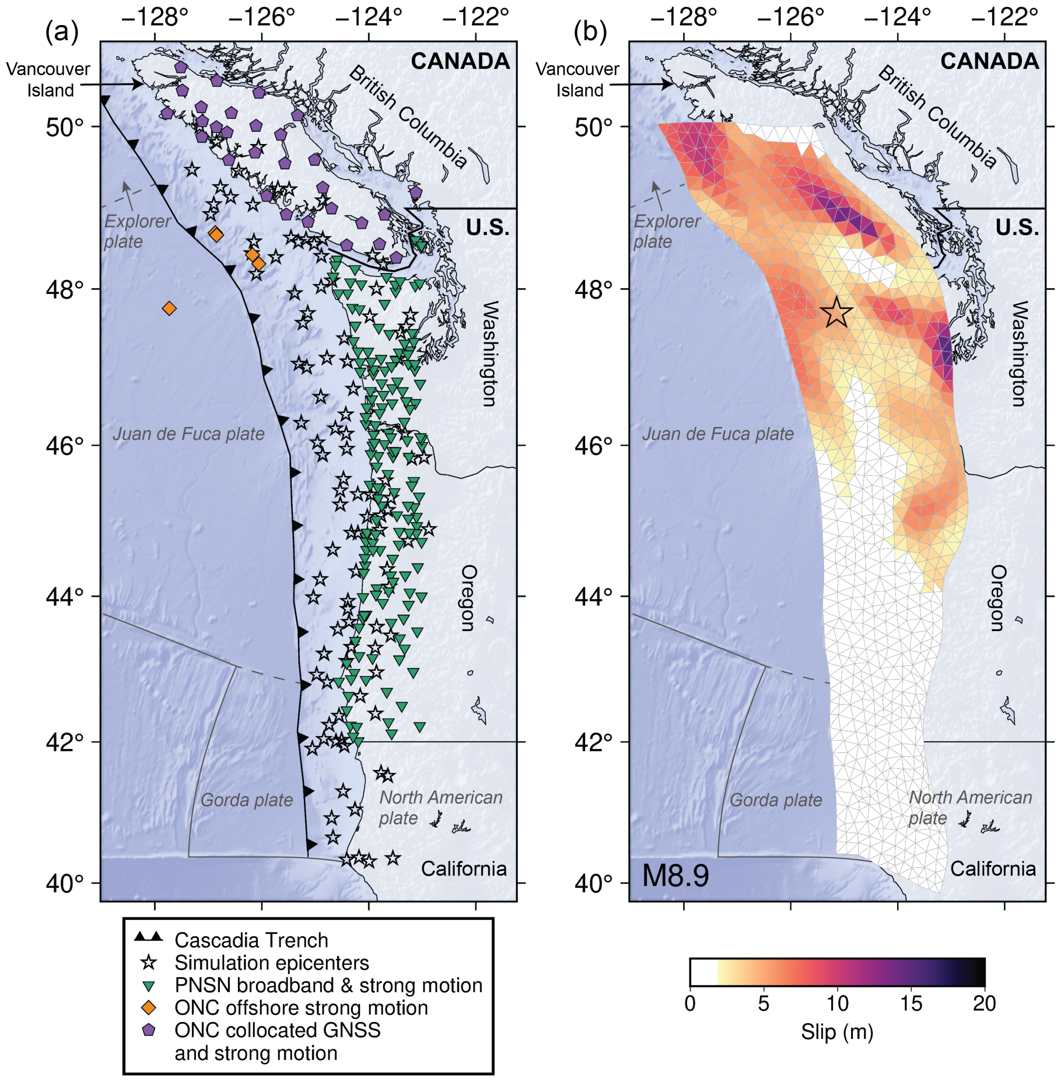

Figure 1 (a) Cascadia Subduction Zone study region with simulated event epicenters (stars) and the network of High-Rate Global Navigation Satellite System (GNSS) and seismic stations (colored by station network and type) used for waveform simulation. PNSN: Pacific Northwest Seismic Network, ONC: Ocean Networks Canada. (b) Example stochastic rupture scenario generated using *FakeQuakes*, plotted on top of the slab mesh.

cation estimate from seismic data (Crowell et al., 2016; Murray et al., 2023). The Solution Aggregator aggregates source info from the three algorithms, which is fed into EQinfo2GM to estimate shaking intensity (Thakoor et al., 2019). Around 1,400 seismic stations and 1,100 GNSS stations can contribute to ShakeAlert at any given time (McGuire et al., 2025).

Ocean Networks Canada (ONC) developed an EEW system for southwestern British Columbia, Canada (hereafter, ONC-EW; Schlesinger et al., 2021) in a collaborative effort with Natural Resources Canada (NRCan), which has been operational since 2023 (McMartin, 2025). The network configuration used for ONC-EW is leading edge as it comprises collocated High-Rate Global Navigation Satellite System (GNSS) and strong-motion sensors, which only exists for a handful of sites around the world (Schlesinger et al., 2021). This unique network configuration allows for onsite combination of high-frequency seismic data with unsaturated geodetic data via a Kalman filter, without the typical time latency transferring information between stations (Bock et al., 2011; Kalman, 1960; Melgar et al., 2013; Rosenberger et al., 2018; Smyth and Wu, 2007). The resulting unbiased displacement and velocity time-series are used for all steps in the EEW system workflow, which includes STA/LTA event detection and P-wave magnitude estimation. Another unique feature of the network configuration is the addition of five subsea strong-motion sensors connected to an underwater cabled network, NEPTUNE (North-East Pacific Time-series Undersea Networked Experiments), which drapes over the CSZ and is the world's first regional multi-node cabled ocean observatory (Barnes and Tunnicliffe, 2008).

Regular EEW system testing ensures continued development and refinement for optimal real-time performance. ShakeAlert and ONC-EW have both undergone various performance evaluations since their rollout, but these have been limited to onshore or small-to-moderate offshore events due to limited data. For example, Böse et al. (2022) assessed the timeliness and accuracy of EPIC and FinDer using **M** < 7.1 onshore crustal earthquakes. Lux et al. (2024) evaluated the overall performance of ShakeAlert, and Babaie Mahani et al. (2023, 2024) evaluated components of ONC-EW, using recorded offshore earthquakes, but their datasets were limited to **M** < 7 events, most of which were neither interface nor intraslab events. Rosenberger et al. (2019b) used a simulation dataset to assess the epicenter location accuracy of ONC-EW, but magnitudes were also limited to **M**7. During the development stage, ONC-EW detected several 3 < **M** < 6.5 offshore events between 2018 and 2020, but none of these events occurred along the CSZ interface (Schlesinger et al., 2021). As the CSZ will inevitably host another **M**8–9 event, it is critical to test the performance of both ShakeAlert and ONC-EW in the event of a large megathrust rupture. To support such efforts, we generate and validate a dataset of moderate to large CSZ earthquakes to ensure robust performance for EEW testing. The overall methodology is outlined in Figure 2 and described in detail in Sections 3–6.

3 Stochastic Rupture Simulations

We curate a simulated dataset for the CSZ consisting of 112 kinematic ruptures and associated waveforms using *FakeQuakes*, an earthquake simulation module from the MudPy repository (Melgar et al., 2016, 2025). Various simulation methodologies exist, ranging from simple stochastic models of high-frequency ground motions (e.g., Boore, 2003) to complex deterministic models involving numerical simulations of full waveform propagation through 3D velocity structure (e.g., Komatitsch and Tromp, 1999; Faccioli et al., 1997; Mazzieri et al., 2013). *FakeQuakes* is a 1D semi-stochastic broadband simulation model, which provides more realistic ground motions compared to a simple stochastic model, yet is efficient enough to support large data generation. *FakeQuakes* is not the only existing 1D semi-stochastic model; however, it is preferred for this study, as opposed to other similar models (e.g., SCEC Broadband platform; Maechling et al., 2014), because it allows for P-wave generation (necessary for EEW) and has previously been tested in the Cascadia region (Melgar et al., 2016; Goldberg and Melgar, 2020; Small and Melgar, 2023). Our objective is to assess how well these waveforms perform at replicating reality with respect to key metrics needed for an EEW system, and subsequently test the performance of EEW systems using several example scenarios from the simulated dataset.

3.1 Kinematic rupture models

We use a CSZ slab model (based on Slab2 geometry; Hayes, 2018) and 1D velocity model (Melgar et al., 2016) (Figure S1) to generate ruptures for earthquakes with target magnitudes ranging from **M**6.8–9.5. The finite length and width of each simulated rupture is determined using stochastic rupture dimension-magnitude scaling laws (Blaser et al., 2010), resulting in final magnitudes ranging from **M**6.6–9.4. The slip distribution along the active part of the fault is constructed using a Von Karman autocorrelation function (Mai and Beroza, 2002) and Karhunen-Loéve expansion (LeVeque et al., 2016), and the total slip is the amount of slip required to produce the target magnitude given the dimensions and elastic properties. The kinematics of the event are controlled by the velocity structure and the static slip amplitudes. See Melgar et al. (2016) for full details of the rupture model generation and Text S1 for user-defined parameters applied in this study.

3.2 Simulated waveforms

For each of the simulated events, we generate waveforms for 29 collocated GNSS and strong-motion sites onshore Vancouver Island, 5 cabled array ocean bottom strong-motion sites offshore Vancouver Island, and 157 broadband and strong-motion sites along coastal Washington and Oregon. Metadata for these sites can be found online (Nye et al., 2026). The Vancouver Island sites are a subset of stations operated by ONC to cover the Canadian areas of the CSZ. The Washington and Oregon sites are a subset of the ShakeAlert network configuration, focusing on locations at greatest risk for shaking from CSZ events. The selected stations include coverage of the major cities landward of the CSZ coastline and are located within a few hundred kilometers of the trench.

3.2.1 GNSS waveforms

The waveforms for the GNSS stations are generated using a deterministic (i.e., physics-governed) approach. 1D Green's functions are first computed with a 2 Hz sampling rate for each subfault station pair following the frequency-waveform matrix propagator method of Zhu and Rivera (2002). The Green's functions are then convolved with a "Dreger" source time function (Melgar et al., 2016), corrected for a moment tensor with appropriate strike and dip for the prescribed slab structure, multiplied by slip on each subfault, and summed to form a single waveform for each event-station pair.

3.2.2 Broadband waveforms

A semi-stochastic approach is used to model broadband ground motions, rather than a fully deterministic approach, due to velocity model limitations and to reduce computational cost at higher frequencies. Small-scale velocity features are poorly-resolved with limited offshore instrumentation and would thus not provide meaningful information regarding structural controls on high-frequency radiation. The low frequencies (< 1 Hz) are generated using the deterministic method described in the previous section, and the high frequencies (> 1 Hz) are generated by summing the spectral response for each subfault assuming a random (i.e., stochastic) phase (Graves and Pitarka, 2010, 2014).

$$A_i(f) = \sum_{j=1,M} C_{ij} S_i(f) G_{ij}(f) P(f) \tag{1}$$

The spectrum resulting from slip on a single subfault (A_i) is a function of the radiation scale factor C_{ij}, source spectrum S_i, path attenuation G_{ij}, and high-frequency decay P for subfault *i*, ray type *j*, and frequency *f*.

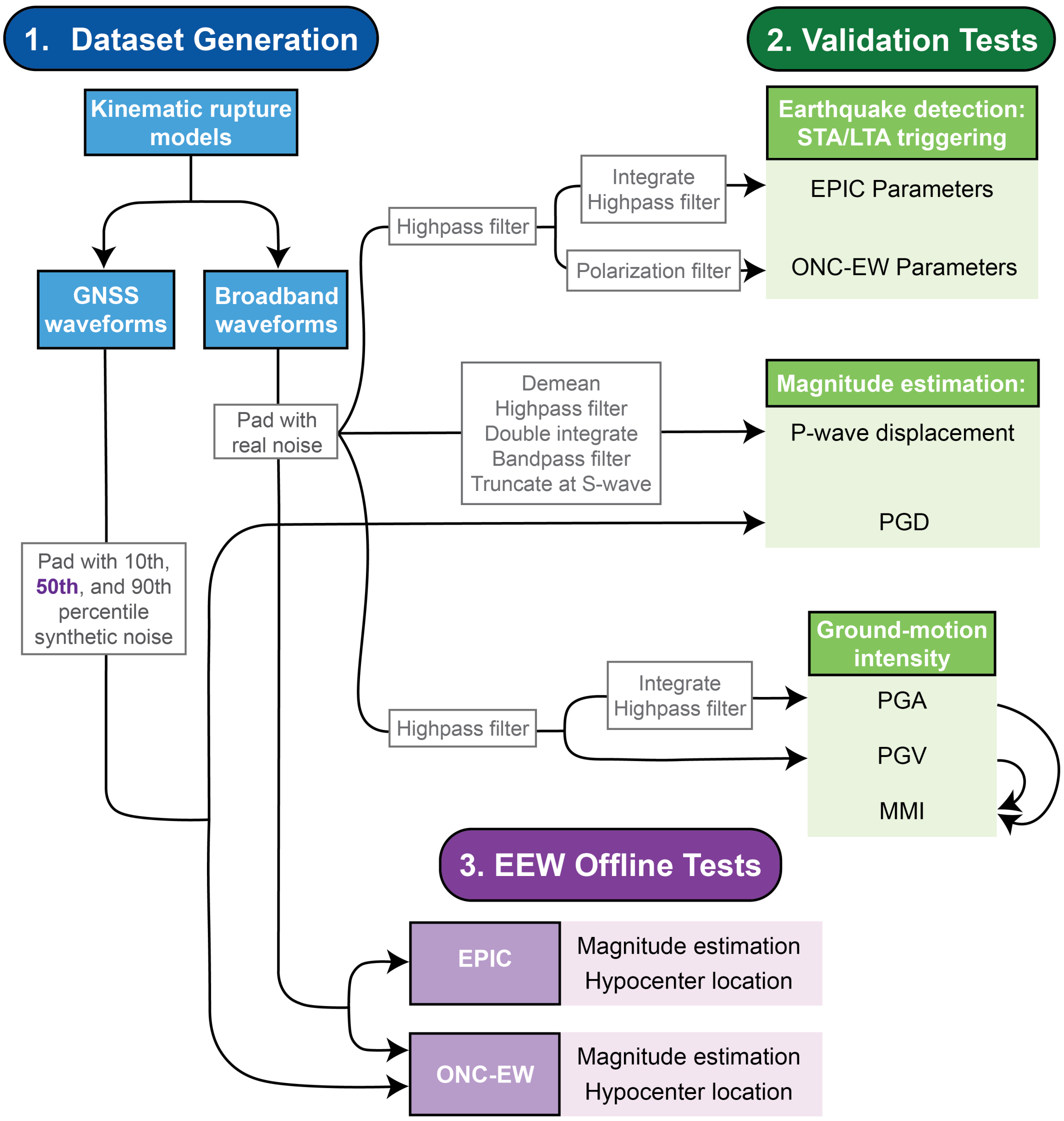

Figure 2 Flowchart outlining the simulated data generation, data processing, and analyses performed in this study. **1. Data Generation** is discussed in Section 3, **2. Validation Tests** is discussed in Sections 4–6, and **3. EEW Offline Tests** is discussed in Section 7.

The low- and high-frequency components are combined to form a full spectrum broadband waveform by first double differentiating the low-frequency displacements to acceleration, after which the two components undergo a matched 4th order causal Butterworth filter. Matched filters apply a lowpass filter to the double-integrated low-frequency displacement waveforms and a highpass filter to the high-frequency acceleration waveforms prior to summation. Following Nye et al. (2024b), we implement a two-frequency matched filter, with a 1 Hz lowpass filter and a 0.1 Hz highpass filter, to reduce an artificial dip in the broadband spectra where the low- and high-frequency components are combined (Nye et al., 2024a,b).

3.2.3 Post-processing

We apply minor post-processing to the raw output waveforms from *FakeQuakes* to mimic real-time recordings. Each simulated waveform is prepended with two minutes of zero-padding and combined with noise. For waveforms simulated at onshore broadband and strong-motion sites, segments of real noise are applied. One day of acceleration data (02/20/2022, 02/02/2022, and 02/26/2022) is downloaded from IRIS for the Ocean Networks Canada Onshore Network (OW) stations AL2H, CMBR, and PHRD, respectively, and the noise streams are screened to remove potential earthquake signals or significant noise spikes. Noise subsets from these three stations are randomly selected and demeaned prior to being combined with onshore broadband simulations.

Although seafloor instruments generally have higher levels of environmental noise when compared with land sensors (Hilmo and Wilcock, 2020), NEPTUNE sensors are completely buried and relatively quiet (Text S2; Table S1; Figure S2). However, as oceanic conditions can be highly variable in different environments, one day of acceleration data (10/31/2018) is downloaded from IRIS for each of the five offshore sites. Segments of the noise are randomly selected, demeaned, and added to the respective station's event waveforms.

We apply synthetic noise to the simulated GNSS waveforms using the Melgar et al. (2020) noise model. GNSS noise is more variable over time compared to that of inertial instruments; thus, one day of noise would not be an adequate representation of conditions over long periods of time. Moreover, the synthetic noise model from Melgar et al. (2020) was derived using data from the Cascadia region, rendering it a better average compared to a single day of real GNSS data. We generate 10th, 50th, and 90th percentile noise time-series to simulate low-, median-, and high-noise scenarios. The additional processing steps described in the following sections are applied individually for each analysis.

4 Earthquake Detection

It is vital to effectively detect an earthquake signal in real time because this initiates the workflow of an EEW algorithm and influences the amount of warning time provided to the public. Events are initially detected using an STA/LTA trigger, which is a ratio of averages of the signal amplitude computed over two user defined time periods. If this function surpasses a predetermined threshold, the picker records a trigger. We evaluate the detection success of the simulated data using the *classic_sta_lta* function from the ObsPy Python module (Krischer et al., 2015) with parameters used by EPIC and ONC-EW. EPIC uses STA(s)/LTA(s)/threshold values of 0.05/5/20 on velocity time-series data. ONC-EW uses values of 1/5/4.9 on acceleration time-series data.

For STA/LTA analyses using EPIC parameters, we filter the vertical component of the noise-combined acceleration broadband waveforms using a 0.075 Hz 4th order causal highpass Butterworth filter (Wu and Zhao, 2006). The waveforms are integrated to velocity, and an additional highpass filter is applied. For analyses using ONC-EW parameters, all three components of the noise-combined acceleration waveforms are highpass filtered, followed by an additional polarization filter to isolate the P-wave from the full signal (Baillard et al., 2013; Cua et al., 2009; Flinn, 1965; Rosenberger, 2010, 2019; Ross et al., 2016; Ross and Ben-Zion, 2014; Schlesinger et al., 2021). The summed square of the three filtered components is then run through the STA/LTA picker.

Using EPIC parameters, the STA/LTA picker triggered (i.e., detected an event) for 79% of the recordings, whereas the picker triggered for 99% of the recordings using the ONC-EW parameters (Figure 3). We do not observe a magnitude bias for missed detections; however, most of the missed detections occurred for records with hypocentral distances (R_{hyp}) > 500 km (Figure 3a), which is the case for both sets of STA/LTA parameters. The detection success is also influenced by radiation azimuth (Figure 3b). Most missed detections occurred at directions nearly along-strike. At these orientations, the P-wave signal can be more emergent due to the P-wave radiation pattern, which is also observed with real earthquakes (Kobayashi et al., 2015).

We next analyze the P-wave arrival detection latencies (δ_{arr}) for recordings that triggered the STA/LTA

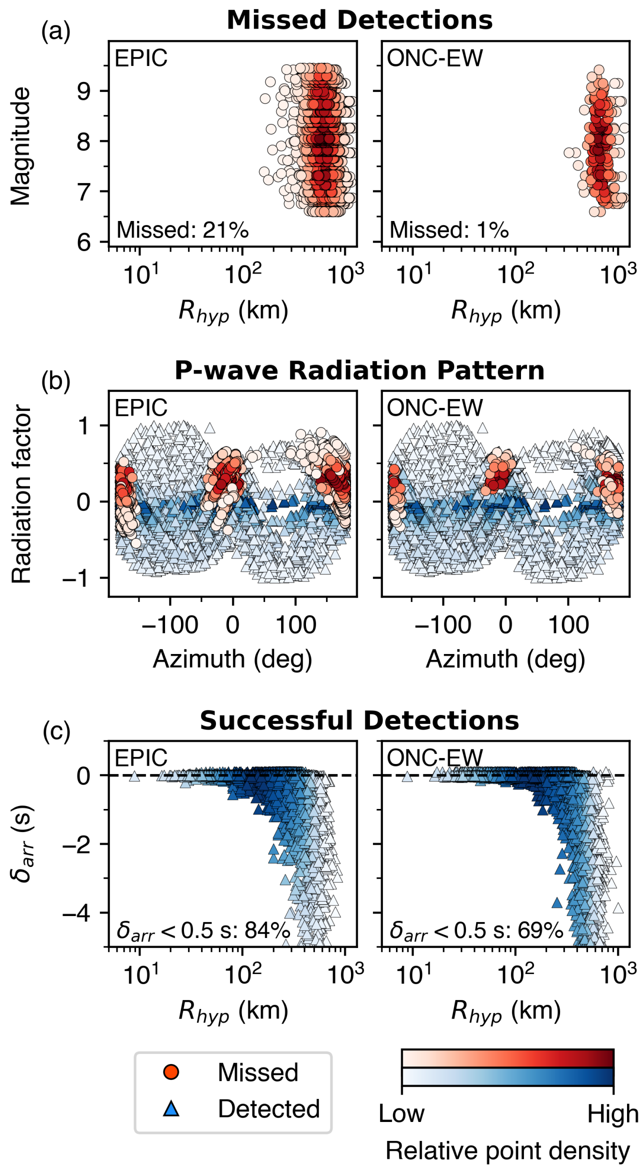

Figure 3 Short-term average/long-term average (STA/LTA) earthquake detection results for the Cascadia simulations using (left) EPIC and (right) ONC-EW STA/LTA configurations. (a) Hypocentral distance (R_{hyp}) and magnitude distribution of missed events, colored by density (red). (b) Records plotted as a function of azimuth and P-wave amplification factor (i.e., radiation pattern), with marker color delineating missed (red color scale) and detected (blue color scale) events. Azimuths of $\sim$0 and $\pm$180 degrees correspond with stations located primarily along strike of the Cascadia Subduction Zone. (c) Detection time residuals (δ_{arr}; true P-arrival minus STA/LTA pick) colored by density (blue) for each simulation that triggered the STA/LTA picker. Residuals are plotted as a function of R_{hyp}, and the zero residuals are indicated by a dashed line. Records with latencies greater than 5 s are not shown.

picker because increased latencies bias location estimates and alert times. δ_{arr} is calculated as the true P-wave arrival time (computed using the ObsPy TauP toolkit and Cascadia velocity model; Crotwell et al., 1999; Krischer et al., 2015) minus the time of the first

STA/LTA trigger occurring on or after the P-wave. The STA/LTA parameters are designed to be highly sensitive to ensure high detection success, which can lead to the picker triggering on noise spikes, even during seismically-quiet periods (Chung et al., 2019). Although aseismic triggering occurs in real-world scenarios, we want to minimize mapping of these artifacts into validation analyses. In real time, an alert would not be issued unless a minimum of four stations recorded a trigger (Chung et al., 2019; Schlesinger et al., 2021).

A significant percentage of records (84% for EPIC parameters and 69% for ONC-EW parameters) have a detection residual < 0.5 s (Figure 3c), which both speaks to the success of the simulations for use in earthquake detection, as well as the success of the parameter configurations themselves. Since the exact arrival times are not known in real time, it is difficult to compare this to the performance of EEW algorithms. However, if we assume an analyst's pick to be accurate, ElarmS (now EPIC) picked arrival times within 0.5 s of the analyst pick times for 89% of their real offshore recordings (Hartog et al., 2016). Our simulated recordings have a slightly lower trigger success, but still perform well in comparison.

Although the STA/LTA picker quickly detected earthquakes on most recordings, there is a negative δ_{arr} distance bias, especially for records with $R_{\text{hyp}} \geq 250$ km (Figure 3c). For a subset of the records, the STA/LTA picker triggered on the S-wave rather than the P-wave because the P-wave was too weak compared to the background noise for the STA/LTA parameter configuration (Figure S3). EPIC has a check in place to prevent S-wave triggers from being associated with an event, which looks at the velocity amplitude range ratio of the horizontal-to-vertical components for a small time window following the trigger (Chung et al., 2019).

The application of a polarization filter in the ONC-EW analysis results in a significant improvement in number of recordings triggered, yet also results in greater latencies between the true arrival time and the pick time. Most of the recordings with larger δ_{arr} using ONC-EW parameters occur at R_{hyp} > 500 km. At these distances, it would take around 1.5+ minutes for stations to trigger, and they would likely not contribute to the source characterization and alert levels. Allen and Melgar (2019) do caution that this type of P-detector may only be useful for borehole sites because soil response at free-field stations could reduce the quality of the filtered data. As near-surface soil response is not included in our simulations, we cannot evaluate this claim.

5 Magnitude Estimation

Once an event is created, source parameters, including magnitude, are estimated. Initially, the magnitude estimate is derived using the first 4–5 seconds of the P-wave, which provides information about the growing source (Kodera, 2018). The displacement amplitude (P_d) of P-waves is a common metric because it has been shown to scale with magnitude for small-to-moderate earthquakes (e.g., Kuyuk and Allen, 2013; Zhang et al., 2022). Magnitude estimation from seismic P-waves is subject to saturation for larger events due to limitations in inertial instruments and seismic processing, which presents challenges for effective alerting of a major megathrust event. GNSS-derived PGD does not suffer from magnitude saturation and can provide better constraints on ground-motion estimates for large earthquakes (Ruhl et al., 2019). Although not *deterministic* of earthquake magnitude (i.e., distinguishable within the first few seconds), geodetic data provide *weak deterministic* information as the rupture organizes into a slip pulse (Goldberg et al., 2018; Meier et al., 2021; Melgar and Hayes, 2017). We evaluate both P-wave amplitudes and PGD to assess simulation magnitude estimation reliability.

5.1 P-wave displacement

P_d is measured as the maximum amplitude of the displacement P-wave over some time interval of several seconds following the P-arrival. Earthquake magnitude has been shown to scale linearly with $log_{10}(P_d)$ and log_{10}(distance) for events with magnitudes $\mathbf{M} \leq$ 7–8, depending on the time window used to calculate P_d (e.g., Crowell et al., 2013; Goldberg and Melgar, 2020; Kuyuk and Allen, 2013; Trugman et al., 2019; Wurman et al., 2007). Goldberg and Melgar (2020) validated magnitude scaling of P_d using a *FakeQuakes* Cascadia dataset to better constrain the empirical $\mathbf{M}$-P_d scaling from Trugman et al. (2019) for magnitudes $\mathbf{M} \geq 7$, though they did not include noise in their simulations. We find it valuable to re-perform the analyses using noisy simulations to ensure equivalent comparison with empirical data.

We process the simulated waveforms following the methodology of Trugman et al. (2019) and Goldberg and Melgar (2020), which includes demeaning the recordings, applying a 0.075 Hz 4$^{\text{th}}$ order causal highpass Butterworth filter, double integrating from acceleration to displacement, and applying an additional bandpass filter between 0.075–3 Hz. We also truncate the recordings at 95% the S-wave arrival time to avoid S-wave contamination. The records are normalized to 10 km R_{hyp} (Goldberg and Melgar, 2020), and P_d is calculated on the vertical components as the maximum amplitude within windows of 4, 6, 12, and 20 s following the P-wave arrival.

The simulation P_d values generally match the amplitude and magnitude-scaling patterns present in the Trugman et al. (2019) observational dataset, especially for the 4 s time window (Figure 4). There is a distinct distance bias for individual events, where larger distance records exhibit lower normalized P_d values. This was also observed by Kuyuk and Allen (2013). Although all records are corrected to a uniform distance, this only accounts for geometric spreading effects; anelastic attenuation also contributes to observed ground-motion trends at larger distances. The Kuyuk and Allen (2013) P_d-magnitude scaling (currently implemented in both EPIC and ONC-EW) was derived using data within 250 km epicentral distance, and EPIC only includes data from stations within 200 km of the calculated epicenter (Chung et al., 2019) for magnitude estimation. If we only consider records within 200 km epicentral distance (as with the Trugman et al. (2019) dataset), the event means and variance closely match empirical trends for time windows < 20 s.

When calculated over the longer 20 s time window, P_d from our simulations do not exhibit the same degree of magnitude saturation suggested by the limited large-magnitude observations and by the Goldberg and Melgar (2020) simulations. A key deviation in our methodology is the use of a two-frequency matched filter for broadband simulation. Goldberg and Melgar (2020) used a uniform corner frequency for the lowpass and highpass filters. The implementation of a two-frequency approach increases energy in the simulated recordings by reducing an artificial dip in the spectra (Nye et al., 2024a), likely contributing to the decreased magnitude saturation. We recognize that this method also adds additional energy outside the bounds of the dip due to filter roll off, primarily for the smaller events in our dataset. It is difficult to ascertain which matched filter implementation is more physically realistic with such limited near-field observations of large earthquakes. Regardless, we find that the simulations exhibit expected trends in P_d evolution, where P_d increases with increased measurement time window and larger magnitudes are better resolved when longer P-wave windows are available. For time windows considered in EEW (~4–5 s), the simulations behave as expected.

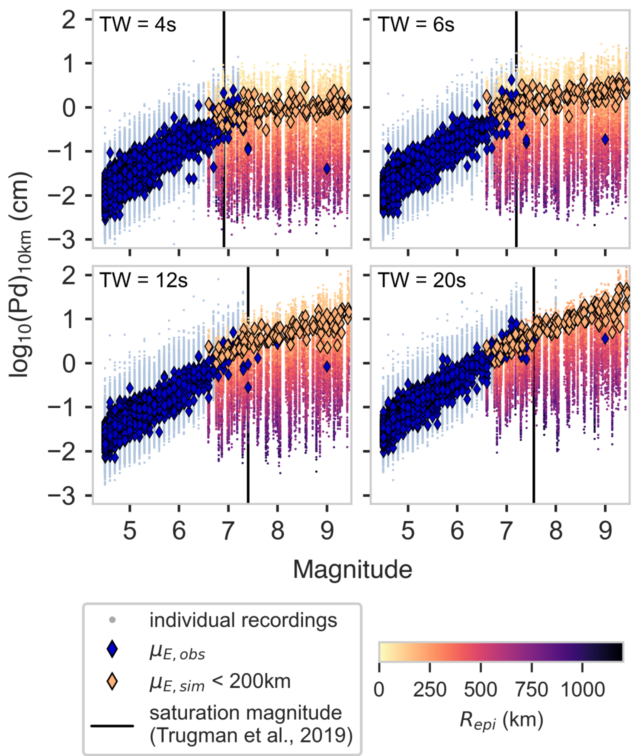

Figure 4 P-wave displacement amplitudes (P_d) measured over time windows of 4, 6, 12, and 20 s. P_d is corrected to 10 km hypocentral distance. The dots indicate individual recordings, whereas the diamonds indicate event means for observations ($\mu_{E,obs}$) and simulations ($\mu_{E,sim}$). Blue markers are the Trugman et al. (2019) observational dataset. The individual simulation values are colored by epicentral distance (R_{epi}), but the event means are calculated only using records within 200 km R_{epi}. The black lines represent the saturation magnitudes predicted by the Trugman et al. (2019) model.

5.2 Peak ground displacement

We evaluate the effects of different GNSS noise levels on simulated PGD and how these values compare with ground-motion model (GMM) estimates. The overlap in frequency content between GNSS signals and noise hinders effective noise filtering unlike seismic data. It is reasonable to assume observed PGD measurements, and subsequently the GMM models regressed on such datasets, are biased by GNSS noise, especially for smaller magnitude events.

PGD is computed on the three-component GNSS displacement seismograms (Goldberg et al., 2021; Melgar et al., 2015) from the collocated ONC sensors.

$$PGD = max\left(\sqrt{N(t)^2 + E(t)^2 + Z(t)^2}\right) \tag{2}$$

Although both GFAST-PGD and ONC-EW rely on the Crowell et al. (2013) GMM, we compare simulated PGD with the Goldberg et al. (2021, hereafter GA21) model, which contains the most up to date PGD scaling coefficients and considers the generalized mean rupture distance (R_p). R_p better accounts for fault finiteness of large ruptures and slip heterogeneity compared to the more commonly used R_{hyp}, and it has shown to better represent unilateral ruptures (Goldberg et al., 2021).

$$R_p = \left(\sum_{i=1}^{n} w_i R_i^p\right)^{1/p} \tag{3}$$

Here, n is the number of subfaults, w_{i} is the weight of the ith subfault, R_{i} is the distance to the ith subfault, and p is the power of the mean. Goldberg et al. (2021) derived three sets of coefficients for datasets consisting of only observed events, only simulated events, and a joint observed-simulated dataset. Cascadia simulations were added to constrain large magnitude events; however, their simulated dataset also did not contain any noise. To avoid circular validation, we compare our simulated PGD with estimates using their GMM derived using only observational data.

$$\begin{aligned}\log_{10}(\mathrm{PGD}) = &-3.841 + 0.919(M) \\ &- 0.122(M)\log_{10}\left(R_P^{-4.5}\right)\end{aligned} \tag{4}$$

PGD residuals are calculated as the natural logarithmic residual ln(GMM PGD/simulated PGD). In this way, negative and positive residuals indicate over- and under-prediction of simulated ground motions, respectively. Well-modeled ground motions should not exhibit bias with model parameters, such as magnitude or distance.

Raw GNSS waveforms without the addition of noise present systematically lower PGD than estimated by GA21, with lower magnitude and larger R_{hyp} records exhibiting the greatest bias (Figure 5a). The means of these residuals are mostly between 0.5–1 natural log unit, but individual record residuals range above 2 natural log units. Melgar et al. (2016) observed a bias in PGD from *FakeQuakes* simulations, but their recordings were larger than estimated using the Melgar et al. (2015) PGD GMM model, directly opposing residual trends from this study. Note that they compute residuals as ln(simulated PGD/GMM PGD), so although their residuals are mostly positive, they have a different implication from the positive residuals we observe. They also observed greater misfit for large magnitude events. This discrepancy between our study and Melgar et al. (2016) could be due to the difference in PGD GMMs used for validation. *FakeQuakes* has also undergone many modifications since its initial publication, which could further contribute to the difference in residual trends. A more recent study compared simulations generated using *FakeQuakes* (1D velocity structure) and *SW4* (3D velocity structure) with observations from several Japanese events (Fadugba et al., 2024). They observed PGD residuals more in line with those in this study, where they are primarily positive and exhibit a distance bias. They attributed the overall bias to the simplification of the earth structure using a 1D velocity model as the 3D simulations had greatly improved residuals, although still systematically positive.

The presence/absence of GNSS noise also contributes to the apparent PGD bias, where residuals from smaller magnitude and larger distance records become more negative with increased noise levels (Figure 5b–d). With the addition of 10th percentile (low) noise, PGD residuals are reduced for records with $\mathbf{M} < 8$ and $R_{hyp} > 200$ km; PGD from all other records is primarily unaffected (Figure 5b). For smaller magnitude events, even this low noise level masks true PGD, but the means mostly fall within GMM uncertainty across the distance range. With the addition of 50th percentile (median) noise, simulated PGD is well-modeled (i.e., residual binned means are near zero) for records with $R_{hyp} < 400$ km, though our dataset exhibits greater variability than the observational dataset used to constrain the model. Residuals from low magnitude and large R_{hyp} records are increased. Lastly, with the addition of 90th percentile (high) noise, the residuals are mostly negative, indicating the noise levels mask true PGD for nearly all records (Figure 5d). With increasingly high noise levels, the signal-to-noise ratio (SNR) becomes too low to distinguish the signal from background noise (Text S3; Figure S4).

Geodetic data are challenging for both modeling and real-time analyses because they are highly sensitive to complex 3D structure, and elevated instrument noise complicates data quality assessment. Even though data used for the GA21 model underwent a manual inspection to reduce bias from poor quality records, a more in-depth quality control, such as one involving SNR, was not used. Furthermore, PGD scaling laws are based on a point source assumption, which breaks down for events with $\mathbf{M} \geq\sim 6$, well below the magnitudes of the events in our dataset. Considering these factors, we find the simulated GNSS data with median noise levels to be well-modeled overall.

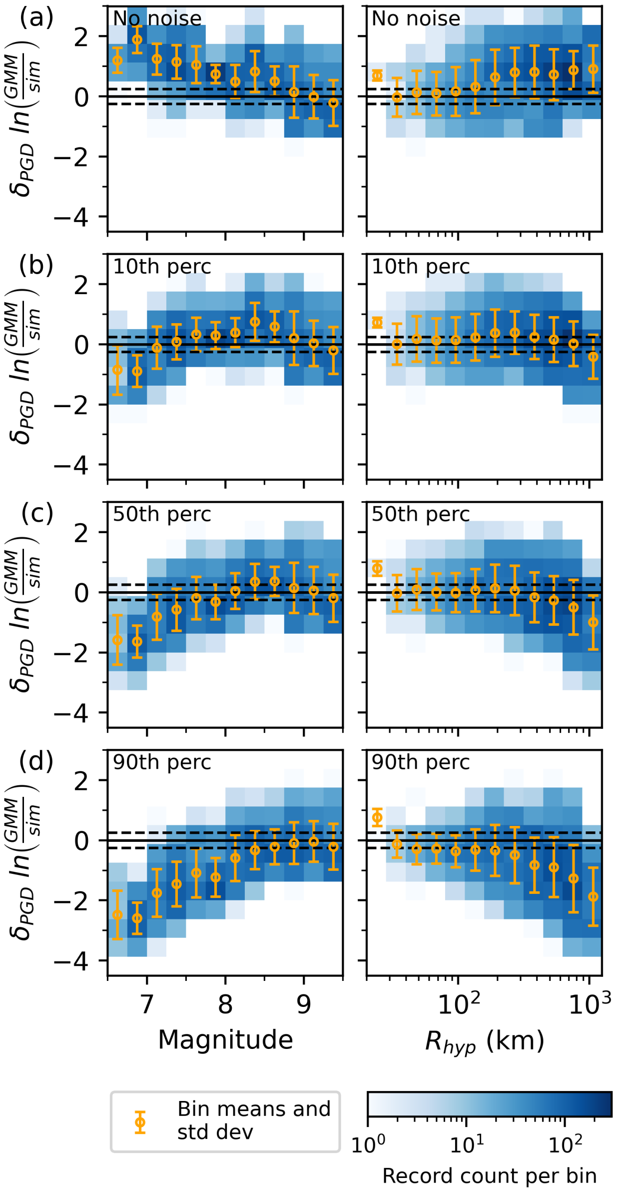

Figure 5 PGD Residuals (δ_{PGD}) between ground-motion model estimates (GMM) and simulated ground motions (sim) as a function of magnitude and hypocentral distance (R_{hyp}) with (a) no noise added, (b) 10th percentile noise added, (c) 50th percentile noise added, and (d) 90th percentile noise added. The markers indicate binned residual means and standard deviations, and the dashed black lines represent the standard deviation for GA21.

6 Ground-motion intensity

Most earthquake early warning studies report performance levels based on the timeliness and accuracy of epicenter location and source characterization. These features, although crucial for effective earthquake alerts, omit a key component of early warning—the ground-motion predictions themselves. Meier (2017) proposed the best early warning metric to be ground-motion prediction error as a function of warning time. If simulated earthquake data are included in EEW development and testing, it is necessary that they adequately capture the expected distribution of ground shaking.

ShakeAlert and ONC-EW ground-motion forecasts are expressed as MMI levels using information from source characterization (McGuire et al., 2025; Schlesinger et al., 2021). MMI contour products are produced by first calculating PGA and PGV GMM distance curves using the event magnitude estimate. These are converted to MMI curves using the Worden et al. (2012) ground-motion-to-intensity conversion equations (GMICEs), where MMI is a linear function of the logarithm of peak ground motion, logarithm of source-to-site distance, and earthquake magnitude. The $\mathrm{MMI}_{\mathrm{PGA}}$ and $\mathrm{MMI}_{\mathrm{PGV}}$ curves are averaged together using a specified weighting to produce a single MMI distance curve. Although MMI is the public-facing intensity measure used for EEW alerts, we focus our analyses on the instrumental ground motions PGA and PGV. A brief MMI analysis is additionally included to assess whether potential instrumental biases are directly translated into MMI biases using the GMICE.

6.1 Peak ground acceleration and peak ground velocity

We follow standard signal processing procedures prior to computing PGA and PGV on the broadband waveforms. A 0.075 Hz 2$^{\text{nd}}$ order acausal highpass Butterworth filter is applied to the acceleration waveforms (Wu and Zhao, 2006), after which they are integrated to velocity and highpass filtered a second time. The simulated PGA and PGV values are computed on the RotD50 (Boore, 2010) of the horizontal components and are compared with estimates from the Next Generation Attenuation Subduction (hereafter NGA-Sub; Parker et al., 2020) ground-motion model. Ideal circumstances would allow for direct comparison of simulated recordings with observed events in the region of interest to ensure unique regional conditions are captured. However, limitations imposed by the dearth of interface events in the CSZ require comparison of the simulated ground motions with estimates from empirical models. Empirical models are still a suitable validation benchmark, especially if the model was developed using solely data from the study region because they reflect regional ground-motion trends. NGA-Sub was derived using global interface and intraslab recordings, including intraslab recordings from Cascadia. The model is considered applicable for magnitudes up to **M**9.5 and closest rupture distances (R_{rup}) out to 1000 km, thus suitable for our simulated data ranges.

As with PGD, we evaluate PGA and PGV by computing residuals as ln(GMM/simulated ground motion). Initial analyses showed a substantial negative bias with distance, indicating over-prediction of the simulations (Figure S5). *FakeQuakes* has predominantly been used to generate low-frequency geodetic waveforms, and peak ground accelerations have been minimally validated in previous studies. Goldberg and Melgar (2020) compared simulated PGA with observed values for the 2014 **M**8.1 Iquique, Chile event, and found the mean PGA residuals to be within 0.5 ln unit. However, they presented the entire residual ensemble as a single relation to the mean, so it is unclear whether a distance bias was also observed in their dataset. Furthermore, their 2014 Iquique simulated time-series were within 100–200 km and would be less subject to attenuation variations.

We implement the following adjustments to *FakeQuakes* source code to improve the attenuation relation. (1) Previously, direct arrivals used to generate S-wave packets were taken as the first arriving ray, which was usually the ray turning below the Moho. The deep propagation of these rays results in less attenuation compared to crustal rays. Now, only crustal rays are considered for the direct P- and S-wave arrivals. (2) The geometric spreading term is changed from $1/R$ to $1/R^{1.2}$, where R is the source-to-site distance (Sahakian et al., 2018). (3) Lastly, we add an elastic attenuation term (Q_{C}) with the form $Q_{C,base} f^n$ for modeling Q_{S} attenuation (Farahbod et al., 2016; Pujades et al., 1997). Although this term allows for frequency dependence, we find $Q_c = 150 f^0$ (i.e., $Q_C = 150$) best reduces the attenuation bias. The path attenuation term (G_{ij} in Eq. 1; see Text S1 or Graves and Pitarka (2010) for more information) is computed using the effective S-wave attenuation ($Q_{S,eff}$) (Pujades et al., 1997).

$$Q_{S,eff} = \frac{1}{\frac{1}{Q_S} + \frac{1}{Q_C}} \quad (5)$$

Anelastic attenuation values are reduced in the velocity model to account for the addition of the elastic attenuation term. The results in the previous sections are based on the updated source code (Melgar et al., 2025) and velocity model.

With these modifications, PGA and PGV are reasonably modeled by the simulations (Figure 6a). Overall, the residual means and standard deviations for both PGA and PGV fall within the expected uncertainty of the NGA-Sub model out to $\sim$700–800 km rupture distance. Beyond this distance range, simulated ground motions are systematically overpredicted, which may contribute to the moderate magnitude bias. As R_{rup} is the distance to the closest point on the fault, large values are only associated with smaller sources. Although NGA-Sub is considered applicable for distances out to 1000 km, the regression dataset does not include any Cascadia interface events, and it is more sparse at the upper end of the distance range. Additionally, the magnitude-dependence of the bias suggests a potential trade-off between NGA-Sub geometric spreading and anelastic attenuation coefficients as the geometric spreading term scales with magnitude. Beyond biases associated with GMM limitations, the simulation framework may also contribute to the observed residual trends. Structurally, 1D velocity models are unable to simulate complex 3D structure and wave propagation inherent in real data (Fadugba et al., 2024). The stronger residual bias and sensitivity of PGV to frequencies around the matched filter suggest that the matched filter implementation may also be a contributing factor. Irrespective of the source of the bias, records at these distances would not contribute to early alerts.

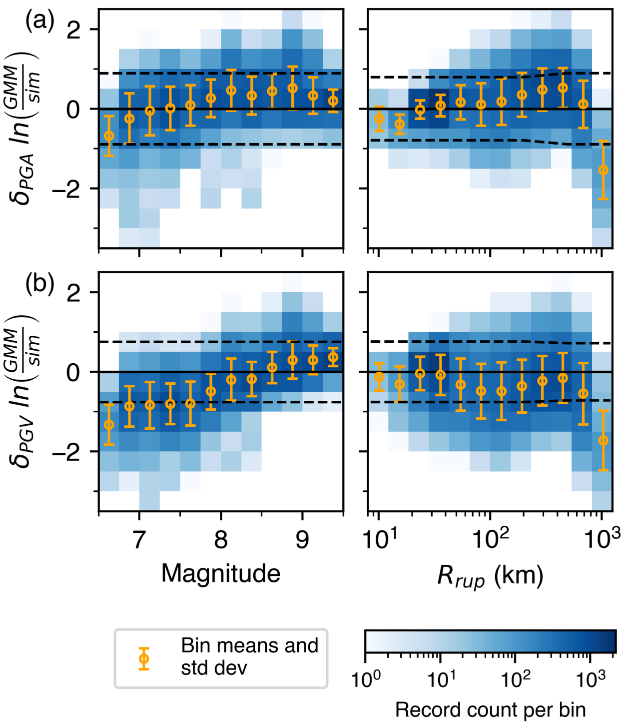

Figure 6 Residuals between ground-motion model estimates (GMM) and simulated ground motions (sim) for (a) PGA (δ_{PGA}) and (b) PGV (δ_{PGV}) as a function of magnitude and closest rupture distance (R_{rup}). The markers indicate the bin residual means and standard deviations, and the dashed black lines represent the maximum standard deviation for NGA-Sub (Parker et al., 2020).

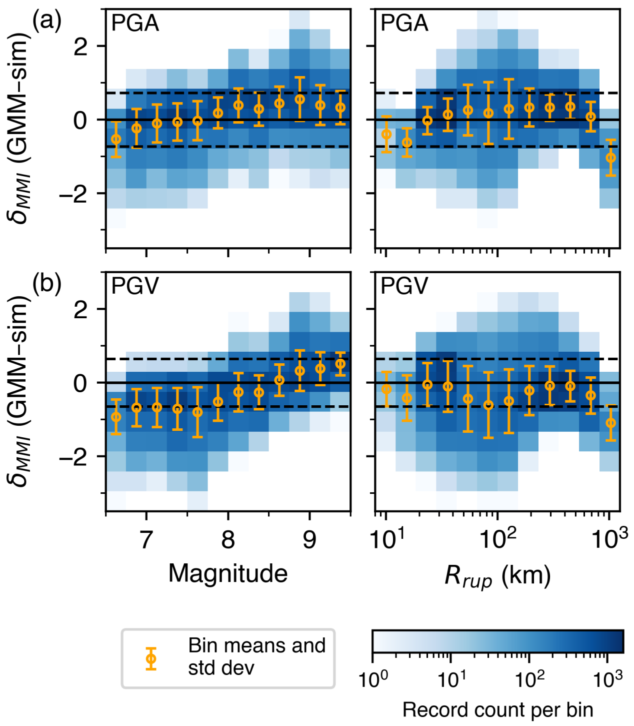

Figure 7 MMI residuals (δ_{MMI}) between ground-motion model estimates (GMM) and simulated ground motions (sim) for (a) MMI computed using PGA scaling and (b) MMI computed using PGV scaling as a function of magnitude and closest rupture distance (R_{rup}). The markers indicate the binned residual means and standard deviations, and the dashed black lines represent the standard deviation for Worden et al. (2012).

6.2 Modified Mercalli intensity

We convert both simulated and NGA-Sub-predicted PGA and PGV to MMI using the Worden et al. (2012) GMICE. Although $\mathrm{MMI_{PGA}}$ and $\mathrm{MMI_{PGV}}$ would be averaged for EEW products, we evaluate these metrics individually. MMI residuals are calculated as the linear residual (GMM MMI - simulated MMI). Similar to PGA and PGV, MMI residual binned means and standard deviations fall mostly within the expected uncertainty of the Worden et al. (2012) GMICE (Figure 7). Both $\mathrm{MMI_{PGA}}$ and $\mathrm{MMI_{PGV}}$ exhibit a moderate magnitude bias, but there appears to be a less-apparent correlation with the bias at large distances compared to PGA and PGV. Nevertheless, the similarity of the residual trends between instrumental and macroseismic intensity measures confirms additional biases are not introduced through the GMICE.

6.3 Ground-motion summary

Considering the infrequency of large subduction zone earthquakes, GMMs for such events are regressed on sparse global datasets, and estimates from such models have both high epistemic uncertainty (poor resolution due to small number of events) and high aleatory uncertainty (regional variations not accounted for in the models). We recognize that ensuring our simulated data are reasonably modeled by such a GMM may result in poor representation of individual study regions. For example, Atkinson and Boore (2003) find that ground motions recorded at geologically similar sites from similar events in Cascadia and Japan exhibit amplitude differences of more than a factor of two. Nevertheless, we believe these generalized ground motions are sufficient for EEW testing purposes, and they can be further improved upon as more large earthquakes are recorded in the future.

7 EPIC and ONC-EW Performance Analysis

The previous validation analyses demonstrate the success of using a 1D semi-stochastic model to simulate waveforms that capture important features necessary for EEW testing. We now present an example of their implementation for EEW performance analysis by running a subset of the scenarios through EPIC and ONC-EW offline systems. We limit the analysis to six scenarios due to the computational expense of running offline tests, but we recommend using the full dataset if conducting a comprehensive analysis. The EPIC event detection boundary extends from California northward through most of Vancouver Island (Kohler et al., 2020), whereas the ONC-EW detection grid is concentrated north of Oregon (Schlesinger et al., 2021). We select two ~**M**7, 8, and 9 events (six total) with either hypocenters or peak slip patches located above a latitude of 46°N

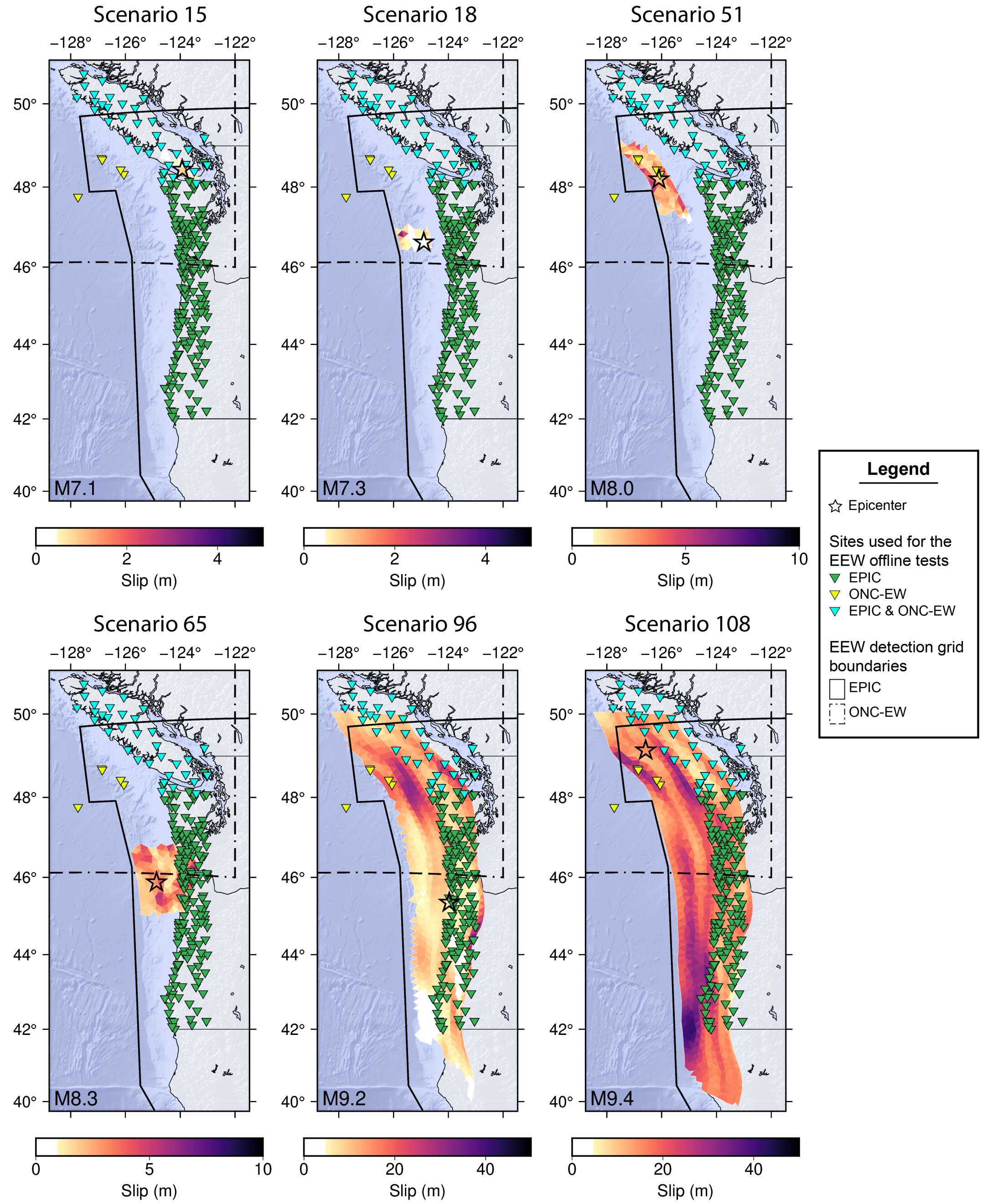

Figure 8 Slip patterns of the six scenario events tested with the EPIC and ONC-EW early warning algorithms. The epicenters are indicated by the stars on each plot. The sites are indicated by triangles and are colored by the early warning system(s) they contributed to. The solid and dashed polygons are the detection grid boundaries for EPIC and ONC-EW, respectively.

to replicate scenarios where ideally both EEW systems would be activated (Figure 9). Recordings for the land-based PNSN and ONC sensors are used for the EPIC tests because ShakeAlert plans to extend their coverage to include ONC sites. Only recordings from ONC sensors (onshore and offshore) and six PNSN sensors located near Vancouver Island are included for the ONC-EW tests because these are the stations currently used for their alerts. The addition of more data would exponentially delay ONC-EW alerts due to the algorithm configuration. GNSS simulations with 50^{th} percentile noise are incorporated for the ONC-EW tests.

EPIC and ONC-EW both detected each of the trial events, which demonstrates improved EEW algorithm performance compared to older versions (e.g., Chung et al., 2019). Several offshore events were previously missed or incorrectly characterized due to the sparse network coverage in Oregon and Washington compared to California (Chung et al., 2019). These earthquakes were smaller in magnitude compared to the scenario events in this study. Another known challenge for point source algorithms is that large events are sometimes split into separate events (Hartog et al., 2016), which can significantly affect the issued alerts. None of the six trial events in this study were recorded as split events. Recently, the EPIC algorithm was modified to disallow triggers from stations at distances > 200 km from being used in any new event associations while the current one is active, which proves to successfully reduce split events (Williamson et al., 2026).

The evolution of magnitude estimation for the events is shown in Figure 9. For the ∼**M**7 events (i.e., scenario events 15 and 18), the maximum magnitudes estimated by EPIC are within 0.1 magnitude unit of the true event magnitudes. For the ∼**M**8, 9 events (i.e., scenario events 51, 65, 96, and 108), the maximum reported magnitudes by EPIC are within two magnitude units of the true magnitudes. For these scenarios, EPIC underestimates the true magnitude and saturates between **M**6.5–7. This saturation is expected because the P_d scaling relation used by EPIC is based upon the first 4 seconds of the P-wave (Kuyuk and Allen, 2013), which can only resolve magnitudes up to ∼**M**7 (Figure 4). This is a common limitation for point source algorithms dependent solely on seismic data, but the magnitude estimates of ONC-EW show a sizable improvement with their joint seismic-geodetic algorithm.

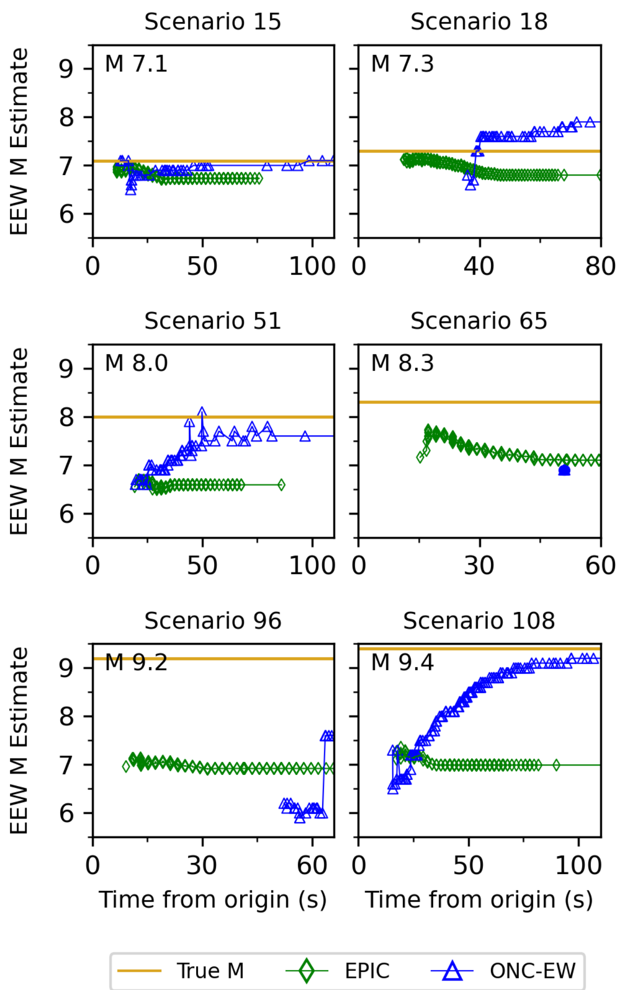

Figure 9 Magnitude estimate evolution for six scenario events using the offline systems for EPIC and ONC-EW.

Although ONC-EW resolves the true magnitude of scenario event 15, it overestimates the magnitude for event 18 by 0.5 magnitude unit, which could be due to the presence of noise in the GNSS data. With the addition of 50th percentile noise, PGD is on average two natural log units larger than expected for an **M**7 event (Figure 5). This no longer appears to bias magnitude estimation for the ∼**M**8, 9 events. However, ONC-EW significantly under-reported the magnitudes of scenarios 65 and 96, which initiated south of their network and detection grid. The initial magnitude estimates for these events were delayed due to the travel time to reach the ONC-EW network stations. For scenario 65, geodetic data did not contribute to event estimation, so only seismic P_d was considered. It is not clear why the geodetic data did not contribute nor why only one magnitude estimate was reported. This warrants further investigation by ONC. Even though scenario 96 was a full margin rupture, it ruptured bilaterally, and the southern extent of the rupture propagation was not captured by the limited ONC network coverage. Inclusion of more PNSN stations near the southern border of the detection grid could improve detection time and magnitude estimation, but the current ONC-EW algorithm is unable to support large networks.

We did not include earthquake location estimation as a component of the validation tests in the previous sections because location accuracy is highly sensitive to network configuration, and our dataset did not include the full network of stations operated by EPIC and ONC-EW. However, offline tests show that EPIC and ONC-EW are mostly able to resolve simulation epicenters within several kilometers, even with the limited network configuration (Figure 10). Both EEW systems use a direct grid search algorithm, and ONC-EW additionally uses a linear least squares algorithm for epicenter location (Chung et al., 2019; Rosenberger et al., 2019a; Schlesinger et al., 2021). For the scenario events, the maximum EPIC location error (scenario 51) is within 8 km and quickly resolves a final epicenter estimate within 2 km of the true epicenter, which is consistent with the median error reported for crustal events in California (Chung et al., 2019). ONC-EW estimates are not as well resolved and are less stable compared to EPIC due to the limited stations used to constrain the source information. For scenarios where the full extent of the rupture was within the ONC-EW detection grid (scenario events 15, 18, 51) the epicenter location was resolved within 5 km.

Overall, EPIC and ONC-EW perform well at characterizing large synthetic events considering the ruptures are offshore and are more complex than crustal events in California. EPIC magnitude estimates saturate at larger magnitudes, but the recent addition of the geodetic-based algorithm GFAST-PGD can provide more reliable magnitude estimates, as demonstrated by ONC-EW. Although the unique configuration of ONC-EW allows for better resolved magnitudes, the smaller network coverage limits resolution of the source characteristics, which can affect alert timing and accuracy for events initiating south of the detection grid (regardless of the final rupture extent). A possible refinement of the EEW algorithms could include implementation of ViDA[3], an early warning algorithm which uses array-based methodology within existing seismic networks to better resolve offshore and out of network events (Ziv et al., 2024).

For this preliminary analysis of Cascadia EEW system

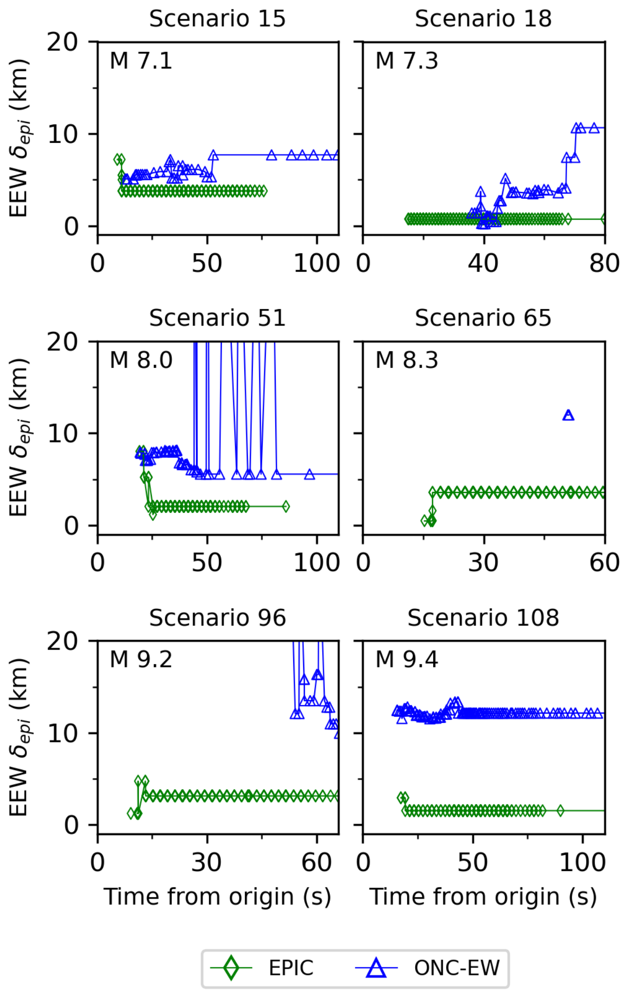

Figure 10 Epicenter location error evolution for six scenario events using the offline systems for EPIC and ONC-EW. Some spikes in ONC-EW epicenter location error extend beyond the scale of the figure.

performance, we did not evaluate ground-motion accuracy. EPIC itself does not report MMI, but rather the ShakeAlert decision module determines MMI contours based on information provided by EPIC, FinDer and G-FAST. ONC-EW allows subscribers to run software code to estimate time left before shaking and MMI given their locations of concern (Schlesinger et al., 2021). It would be valuable to run these simulations through FinDer in a future study because FinDer is better designed to characterize large events compared to the EPIC point source algorithm. Additionally, these scenarios do not include multi-events, such as in the case of foreshocks or aftershocks, which are a challenge for EEW systems. That is beyond the scope of this project but could be an avenue for additional performance testing.

8 Conclusions

Cascadia is a region of high seismic risk, and when a large megathrust earthquake inevitably ruptures, it will leave thousands of unreinforced buildings, bridges, and other critical infrastructure inoperative. In such a scenario, efficient and reliable EEW alerts will be critical for minimizing injuries and disruption. We generate and validate a dataset of moderate-to-large Cascadia ruptures and waveforms using *FakeQuakes* to support continued EEW performance and testing in this region. The simulations are found to be well modeled with respect to key EEW features, including earthquake detection, magnitude estimation, and ground-motion intensity distribution, although there are avenues for further improvement if additional computational resources are available. This could include use of a realistic 3D Earth structure (Fadugba et al., 2024), addition of a coupling model (Small and Melgar, 2021), increased velocity resolution from the Cascadia2021 initiative (Ashraf et al., 2025), and contribution from upcoming Cascadia Region Earthquake Science Center (CRESCENT) efforts. To demonstrate applications of the simulated dataset, six of the scenarios are run through EPIC and ONC-EW offline systems, although we recommend performing an in-depth analysis using all simulations to more comprehensively identify possible challenges that may arise in a large complex rupture of the CSZ.

Acknowledgments

We sincerely thank Martijn van den Ende and one anonymous reviewer for their thoughtful and constructive feedback, which undoubtedly strengthened of the quality of this manuscript. This work was funded in part in collaboration with Ocean Networks Canada on a contract to the University of Oregon, with support from NASA Roses grant 80NSSC21K0841 and USGS EHP grant G23AP00048-00.

Data and code availability

Noise and data streams for ONC-operated onshore and offshore sites were provided by Ocean Networks Canada. Maps were produced using the Generic Mapping Tools software (Wessel et al., 2019) with a digital elevation model downloaded from SRTM30 (Becker et al., 2009). Simulations were generated using MudPy v1.4 simulation codes (Melgar et al., 2025), and all analyses were completed with in-house code, available online at https://github.com/taranye96/cascadia_EEW. Data used to generate the simulated dataset, along with the simulated rupture models and waveforms, are also available online (Nye et al., 2026).

Competing interests

The authors have no competing interests.

References

Aagaard, B. T., Hall, J. F., and Heaton, T. H. Characterization of near-source ground-motions with earthquake simulations. *Earthquake Spectra*, 17(2):177–207, 2001. doi: 10.1193/1.1586171.

Allen, R. M. Earthquakes, Early and Strong Motion Warning. In Gupta, H. K., editor, *Encyclopedia of Solid Earth Geophysics*, Encyclopedia of Earth Sciences Series. Springer, Dordrecht, 2011. doi: 10.1007/978-90-481-8702-7_202.

Allen, R. M. and Melgar, D. Earthquake Early Warning: Advances, Scientific Challenges, and Societal Needs. *Annual Review of Earth and Planetary Sciences*, 47(1):361–388, 2019. doi: 10.1146/annurev-earth-053018-060457.

Ashraf, A., Hooft, E., Toomey, D. R., Tréhu, A., Nolan, S., Wirth, E., and Ward, K. M. A high-resolution 3-D P-wave velocity structure of the south-central Cascadia Subduction Zone from wide-angle shore-crossing seismic refraction data. *Journal of Geophysical Research: Solid Earth*, 130:e2024JB029525, 2025. doi: 10.1029/2024JB029525.

Atkinson, G. and Boore, D. Empirical Ground-Motion Relations for Subduction-Zone Earthquakes and Their Application to Cascadia and Other Regions. *Bulletin of the Seismological Society of America*, 93(4):1703–1729, 2003. doi: 10.1785/0120020156.

Atwater, B. F. Evidence for Great Holocene Earthquakes Along the Outer Coast of Washington State. *Science*, 236(4804):942–944, 1987. doi: 10.1126/science.236.4804.942.

Babaie Mahani, A., Ferguson, E., Crosby, B., Schlesinger, A., Pirenne, B., and Price, E. Estimation of shaking intensity in a few seconds: An earthquake early warning system for southwestern British Columbia, 2023. Paper (356) presented at CCEE–PCEE 2023, 25–30 Jun.

Babaie Mahani, A., Ferguson, E., and Pirenne, B. Magnitude estimation and site characterization in southwestern British Columbia: application to earthquake early warning. *Journal of Seismology*, 28(3):735–751, 2024. doi: 10.1007/s10950-024-10216-5.

Baillard, C., Crawford, W. C., Ballu, V., Hibert, C., and Mangeney, A. An automatic kurtosis-based P and S phase picker designed for local seismic networks. *Bulletin of the Seismological Society of America*, 104(1):394–409, 2013. doi: 10.1785/0120120347.

Barnes, C. R. and Tunnicliffe, V. Building the World's First Multi-node Cabled Ocean Observatories (NEPTUNE Canada and VENUS, Canada): Science, Realities, Challenges and Opportunities. In *OCEANS 2008 - MTS/IEEE Kobe Techno-Ocean*, page 1–8. IEEE, 2008. doi: 10.1109/oceanskobe.2008.4531076.

Becker, J. J., Sandwell, D. T., Smith, W. H. F., Braud, J., Binder, B., Depner, J., Fabre, D., Factor, J., Ingalls, S., Kim, S.-H., Ladner, R., Marks, K., Nelson, S., Pharaoh, A., Trimmer, R., Von Rosenberg, J., Wallace, G., and Weatherall, P. Global Bathymetry and Elevation Data at 30 Arc Seconds Resolution: SRTM30_PLUS. *Marine Geodesy*, 32(4):355–371, 2009. doi: 10.1080/01490410903297766.

Blaser, L., Kruger, F., Ohrnberger, M., and Scherbaum, F. Scaling Relations of Earthquake Source Parameter Estimates with Special Focus on Subduction Environment. *Bulletin of the Seismological Society of America*, 100(6):2914–2926, 2010. doi: 10.1785/0120100111.

Bock, Y., Melgar, D., and Crowell, B. W. Real-Time Strong-Motion Broadband Displacements from Collocated GPS and Accelerometers. *Bulletin of the Seismological Society of America*, 101(6): 2904–2925, 2011. doi: 10.1785/0120110007.

Boore, D. M. Simulation of Ground Motion Using the Stochastic Method. *Pure and Applied Geophysics*, 160(3):635–676, 2003. doi: 10.1007/pl00012553.

Boore, D. M. Orientation-Independent, Nongeometric-Mean Measures of Seismic Intensity from Two Horizontal Components of Motion. *Bulletin of the Seismological Society of America*, 100(4): 1830–1835, 2010. doi: 10.1785/0120090400.

Böse, M., Smith, D. E., Felizardo, C., Meier, M.-A., Heaton, T. H., and Clinton, J. F. FinDer v.2: Improved real-time ground-motion predictions for M2–M9 with seismic finite-source characterization. *Geophysical Journal International*, 212(1):725–742, 2018. doi: 10.1093/gji/ggx430.

Böse, M., Andrews, J., O'Rourke, C., Kilb, D., Lux, A., Bunn, J., and McGuire, J. Testing the ShakeAlert earthquake early warning system using synthesized earthquake sequences. *Seismological Research Letters*, 94(1):243–259, 2022. doi: 10.1785/0220220088.

Böse, M., Andrews, J., Hartog, R., and Felizardo, C. Performance and next-generation development of the finite-fault rupture detector (FinDer) within the United States West Coast ShakeAlert warning system. *Bulletin of the Seismological Society of America*, 113(2):648–663, 2023. doi: 10.1785/0120220183.

Bostock, M. G., Christensen, N. I., and Peacock, S. M. Seismicity in Cascadia. *Lithos*, 332–333:55–66, 2019. doi: 10.1016/j.lithos.2019.02.019.

Butler, R. Cascadia earthquake science and hazards, 2018.

Chamoli, B. P., Kumar, A., Chen, D.-Y., Gairola, A., Jakka, R. S., Pandey, B., Kumar, P., and Rathore, G. A Prototype Earthquake Early Warning System for Northern India. *Journal of Earthquake Engineering*, 25(12):2455–2473, 2021. doi: 10.1080/13632469.2019.1625828.

Chung, A. I., Henson, I., and Allen, R. M. Optimizing earthquake early warning performance: ElarmS-3. *Seismological Research Letters*, 90(2A):727–743, 2019. doi: 10.1785/0220180192.

Clinton, J., Zollo, A., Marmureanu, A., Zulfikar, C., and Parolai, S. State-of-the art and future of earthquake early warning in the European region. *Bulletin of Earthquake Engineering*, 14(9): 2441–2458, 2016. doi: 10.1007/s10518-016-9922-7.

Cooper, J. Earthquake indicator. *San Francisco Bulletin*, 1868.

Crane, S., Seywerd, H., Adams, J., Bird, A., Kolaj, M., and Perry, C. National Earthquake Early Warning for Canada. In *Canadian Conference – Pacific Conference on Earthquake Engineering 2023*, Vancouver, British Columbia, Canada, 2023.

Crotwell, H. P., Owens, T. J., and Ritsema, J. The TauP toolkit: Flexible seismic travel-time and ray-path utilities. *Seismological Research Letters*, 70(2):154–160, 1999. doi: 10.1785/gssrl.70.2.154.

Crowell, B. W., Melgar, D., Bock, Y., Haase, J. S., and Geng, J. Earthquake magnitude scaling using seismogeodetic data. *Geophysical Research Letters*, 40(23):6089–6094, 2013. doi: 10.1002/2013gl058391.

Crowell, B. W., Schmidt, D. A., Bodin, P., Vidale, J. E., Gomberg, J., Renate Hartog, J., Kress, V. C., Melbourne, T. I., Santillan, M., Minson, S. E., and Jamison, D. G. Demonstration of the Cascadia G-FAST geodetic earthquake early warning system for the Nisqually, Washington, earthquake. *Seismological Research Letters*, 87(4):930–943, 2016. doi: 10.1785/0220150255.

Cua, G., Fischer, M., Heaton, T., and Wiemer, S. Real-time Performance of the Virtual Seismologist Earthquake Early Warning Algorithm in Southern California. *Seismological Research Letters*, 80(5):740–747, 2009. doi: 10.1785/gssrl.80.5.740.

Cutts, M., Wang, Y., and Yu, Q. New Perspectives on Building Resilience into Infrastructure Systems. *Natural Hazards Review*, 18 (1), 2017. doi: 10.1061/(asce)nh.1527-6996.0000203.

Faccioli, E., Maggio, F., Paolucci, R., and Quarteroni, A. 2d and 3D elastic wave propagation by a pseudo-spectral domain decomposition method. *Journal of Seismology*, 1(3):237–251, 1997. doi: 10.1023/a:1009758820546.

Fadugba, O., Sahakian, V., Melgar, D., Rodgers, A., and Shimony, R. The Impact of the Three-Dimensional Structure of a Subduction Zone on Time-dependent Crustal Deformation Measured by HR-GNSS. *Seismica*, 3(1), 2024. doi: 10.26443/seismica.v3i1.887.

Farahbod, A. M., Calvert, A. J., Cassidy, J. F., and Brillon, C. Coda Q in the northern Cascadia subduction zone. *Bulletin of the Seismological Society of America*, 106(5):1939–1947, 2016. doi: 10.1785/0120160058.

Flinn, E. Signal analysis using rectilinearity and direction of particle motion. *Proceedings of the IEEE*, 53(12):1874–1876, 1965. doi: 10.1109/proc.1965.4462.

Goldberg, D. E. and Melgar, D. Generation and Validation of Broadband Synthetic P Waves in Semistochastic Models of Large Earthquakes. *Bulletin of the Seismological Society of America*, 110(4):1982–1995, 2020. doi: 10.1785/0120200049.

Goldberg, D. E., Melgar, D., Bock, Y., and Allen, R. M. Geodetic Observations of Weak Determinism in Rupture Evolution of Large Earthquakes. *Journal of Geophysical Research: Solid Earth*, 123 (11):9950–9962, 2018. doi: 10.1029/2018jb015962.

Goldberg, D. E., Melgar, D., Hayes, G. P., Crowell, B. W., and Sahakian, V. J. A Ground-Motion Model for GNSS Peak Ground Displacement. *Bulletin of the Seismological Society of America*, 111 (5):2393–2407, 2021. doi: 10.1785/0120210042.

Goldfinger, C., Nelson, C. H., Morey, A. E., Johnson, J. E., Patton, J. R., Karabanov, E. B., Gutierrez-Pastor, J., Eriksson, A. T., Gracia, E., Dunhill, G., Enkin, R. J., Dallimore, A., and Vallier, T. Turbidite event history—Methods and implications for Holocene paleoseismicity of the Cascadia subduction zone. Professional Paper 1661-F, U.S. Geological Survey, 2012. doi: 10.3133/pp1661F.

Graves, R. and Pitarka, A. Refinements to the Graves and Pitarka (2010) broadband ground-motion simulation method. *Seismological Research Letters*, 86(1):75–80, 2014. doi: 10.1785/0220140101.

Graves, R. W. and Pitarka, A. Broadband Ground-Motion Simulation Using a Hybrid Approach. *Bulletin of the Seismological Society of America*, 100(5A):2095–2123, 2010. doi: 10.1785/0120100057.

Graves, R. W., Aagaard, B. T., and Hudnut, K. W. The ShakeOut Earthquake Source and Ground Motion Simulations. *Earthquake Spectra*, 27(2):273–291, 2011. doi: 10.1193/1.3570677.

Harris, R. A., Barall, M., Lockner, D. A., Moore, D. E., Ponce, D. A., Graymer, R. W., Funning, G., Morrow, C. A., Kyriakopoulos, C., and Eberhart-Phillips, D. A geology and geodesy based model of dynamic earthquake rupture on the Rodgers Creek-Hayward-Calaveras fault system, California. *Journal of Geophysical Research: Solid Earth*, 126(3), 2021. doi: 10.1029/2020jb020577.

Hartog, R. J., Kress, V. C., Malone, S. D., Bodin, P., Vidale, J. E., and Crowell, B. W. Earthquake Early Warning: ShakeAlert in the Pacific Northwest. *Bulletin of the Seismological Society of America*, 106(4):1875–1886, 2016. doi: 10.1785/0120150261.

Hayes, G. Slab2 - A Comprehensive Subduction Zone Geometry Model. U.S. Geological Survey data release, 2018. doi: 10.5066/F7PV6JNV.

Hilmo, R. and Wilcock, W. S. D. Physical sources of high-frequency seismic noise on Cascadia Initiative ocean bottom seismometers. *Geochemistry, Geophysics, Geosystems*, 21(10), 2020. doi: 10.1029/2020gc009085.

Kalman, R. E. A New Approach to Linear Filtering and Prediction Problems. *Journal of Basic Engineering*, 82(1):35–45, 1960. doi: 10.1115/1.3662552.

Kobayashi, M., Takemura, S., and Yoshimoto, K. Frequency and distance changes in the apparent P-wave radiation pattern: Effects of seismic wave scattering in the crust inferred from dense seismic observations and numerical simulations. *Geophysical Journal International*, 202(3):1895–1907, 2015. doi: 10.1093/gji/ggv263.

Kodera, Y. Real-time detection of rupture development: Earthquake early warning using P waves from growing ruptures. *Geophysical Research Letters*, 45(1):156–165, 2018. doi: 10.1002/2017gl076118.

Kohler, M. D., Cochran, E. S., Given, D., Guiwits, S., Neuhauser, D., Henson, I., Hartog, R., Bodin, P., Kress, V., Thompson, S., Felizardo, C., Brody, J., Bhadha, R., and Schwarz, S. Earthquake Early Warning ShakeAlert System: West Coast Wide Production Prototype. *Seismological Research Letters*, 89(1):99–107, 2017. doi: 10.1785/0220170140.

Kohler, M. D., Smith, D. E., Andrews, J., Chung, A. I., Hartog, R., Henson, I., Given, D. D., de Groot, R., and Guiwits, S. Earthquake Early Warning ShakeAlert 2.0: Public Rollout. *Seismological Research Letters*, 91(3):1763–1775, 2020. doi: 10.1785/0220190245.

Komatitsch, D. and Tromp, J. Introduction to the spectral element method for three-dimensional seismic wave propagation. *Geophysical Journal International*, 139(3):806–822, 1999. doi: 10.1046/j.1365-246x.1999.00967.x.

Krischer, L., Megies, T., Barsch, R., Beyreuther, M., Lecocq, T., Caudron, C., and Wassermann, J. ObsPy: a bridge for seismology into the scientific Python ecosystem. *Computational Science & Discovery*, 8(1):014003, 2015. doi: 10.1088/1749-4699/8/1/014003.

Kuyuk, H. S. and Allen, R. M. A global approach to provide magnitude estimates for earthquake early warning alerts. *Geophysical Research Letters*, 40(24):6329–6333, 2013. doi: 10.1002/2013gl058580.

LeVeque, R. J., Waagan, K., González, F. I., Rim, D., and Lin, G. Generating Random Earthquake Events for Probabilistic Tsunami Hazard Assessment. *Pure and Applied Geophysics*, 173(12): 3671–3692, 2016. doi: 10.1007/s00024-016-1357-1.

Lin, J., Melgar, D., Thomas, A. M., and Searcy, J. Early Warning for Great Earthquakes From Characterization of Crustal Deformation Patterns With Deep Learning. *Journal of Geophysical Research: Solid Earth*, 126(10), 2021. doi: 10.1029/2021jb022703.

Lux, A. I., Smith, D., Böse, M., McGuire, J. J., Saunders, J. K., Huynh, M., Stubailo, I., Andrews, J., Lotto, G., Crowell, B., Crane, S., Allen, R. M., Given, D., Hartog, R., Heaton, T., Husker, A., Marty, J., O'Driscoll, L., Tobin, H., McBride, S. K., and Toomey, D. Status and Performance of the ShakeAlert Earthquake Early Warning System: 2019–2023. *Bulletin of the Seismological Society of America*, 114(6):3041–3062, 2024. doi: 10.1785/0120230259.

Madin, I. and Burns, W. Map of earthquake and tsunami damage potential for a simulated magnitude 9 Cascadia earthquake. Technical report, State of Oregon Department of Geology and Mineral Industries, 2013. https://www.wsdot.wa.gov/research/reports/fullreports/896-4.pdf. Report No. O-13-06).

Maechling, P. J., Silva, F., Callaghan, S., and Jordan, T. H. SCEC Broadband Platform: System Architecture and Software Implementation. *Seismological Research Letters*, 86(1):27–38, 2014. doi: 10.1785/0220140125.

Mai, P. M. and Beroza, G. C. A spatial random field model to characterize complexity in earthquake slip. *Journal of Geophysical Research: Solid Earth*, 107(B11), 2002. doi: 10.1029/2001jb000588.

Massin, F., Clinton, F., Marroquin, G., Protti, M., Strauch, W., Yani-Quiyuch, R., Burgoa, B., Munoz, C., Böse, M., Castro, D., Shamble, O., Flores, M., Garita, C., Orihuela, B., Pineda, K., Serrano, J., Talavera, E., and Vega, F. Earthquake early warning in Central America from 2016 to 2024. *Seismological Research Letters*, pages 1–25, 2026. doi: 10.1785/0220250242.

Mazzieri, I., Stupazzini, M., Guidotti, R., and Smerzini, C. SPEED: SPectral Elements in Elastodynamics with Discontinuous Galerkin: A non-conforming approach for 3D multi-scale problems. *International Journal for Numerical Methods in Engineering*, 95(12):991–1010, 2013. doi: 10.1002/nme.4532.

McGuire, J. J., Ulberg, C. W., Lux, A. I., Böse, M., Andrews, J. R., Smith, D. E., Crowell, B. W., Murray, J. R., Henson, I., Hartog, R., Felizardo, C., Huynh, M., Aranha, M., Parker, G. A., Baltay, A., Murray, M. H., Biasi, G. P., Guiwits, S., Saunders, J. K., Good, A. D., Marcelo Santillan, V., Scrivner, C. W., Szeliga, W. M., Melbourne, T. I., Kress, V., de Groot, R. M., McBride, S. K., Given, D., Allen, R. M., Heaton, T. H., Husker, A., Thomas, V., Tobin, H. J., Jha, S., and Bunn, J. ShakeAlert® version 3: Expected performance in large earthquakes. *Bulletin of the Seismological Society of America*, 115(2):533–561, 2025. doi: 10.1785/0120240189.

McMartin, K. Variations in earthquake detection across Ocean Networks Canada's early warning system (Honours thesis. *School of Earth and Ocean Sciences*, 2025.

Meier, M. How "good" are real-time ground motion predictions from Earthquake Early Warning systems? *Journal of Geophysical Research: Solid Earth*, 122(7):5561–5577, 2017. doi: 10.1002/2017jb014025.

Meier, M.-A., Ampuero, J.-P., Cochran, E., and Page, M. Apparent earthquake rupture predictability. *Geophysical Journal International*, 225(1):657–663, 2021. doi: 10.1093/gji/ggaa610.

Melgar, D. Consideration of rupture kinematics increases tsunami amplitudes in far-field hazards assessments. *Seismica*, 2(4), 2026. doi: 10.26443/seismica.v2i4.1668.

Melgar, D. and Hayes, G. P. Systematic Observations of the Slip Pulse Properties of Large Earthquake Ruptures. *Geophysical Research Letters*, 44(19):9691–9698, 2017. doi: 10.1002/2017gl074916.

Melgar, D., Bock, Y., Sanchez, D., and Crowell, B. W. On robust and reliable automated baseline corrections for strong motion seismology. *Journal of Geophysical Research: Solid Earth*, 118(3): 1177–1187, 2013. doi: 10.1002/jgrb.50135.

Melgar, D., Crowell, B. W., Geng, J., Allen, R. M., Bock, Y., Riquelme, S., Hill, E. M., Protti, M., and Ganas, A. Earthquake magnitude calculation without saturation from the scaling of peak ground displacement. *Geophysical Research Letters*, 42:5197–5205, 2015. doi: 10.1002/2015GL064278.

Melgar, D., LeVeque, R. J., Dreger, D. S., and Allen, R. M. Kinematic rupture scenarios and synthetic displacement data: An example application to the Cascadia subduction zone. *Journal of Geophysical Research: Solid Earth*, 121(9):6658–6674, 2016. doi: 10.1002/2016jb013314.

Melgar, D., Crowell, B. W., Melbourne, T. I., Szeliga, W., Santillan, M., and Scrivner, C. Noise characteristics of operational real-time high-rate GNSS positions in a large aperture network. *Journal of Geophysical Research: Solid Earth*, 125(7), 2020. doi: 10.1029/2019jb019197.

Melgar, D., taranye96, Lin, T., Kong, Q., christineruhl, sheng6010, Adair, M., Marfito, B., and LeVeque, R. J. UO-Geophysics/MudPy: v1.4, 2025. doi: 10.5281/ZENODO.15547301.

Murray, J. R., Crowell, B. W., Murray, M. H., Ulberg, C. W., McGuire, J. J., Aranha, M. A., and Hagerty, M. T. Incorporation of real-time earthquake magnitudes Estimated via peak ground displacement scaling in the ShakeAlert earthquake early warning system. *Bulletin of the Seismological Society of America*, 113(3): 1286–1310, 2023. doi: 10.1785/0120220181.

Nakamura, Y. On the urgent earthquake detection and alarm system (UrEDAS. In *Proceedings of the 9th World Conference on Earthquake Engineering*, volume 7, page 673–678, Tokyo-Kyoto, Japan, 1988.

Nye, T., Dybing, S., D., and Sahakian, V. The case of the missing frequencies: Reduction of an artificial spectral deficiency in semistochastic broadband simulation. *Seismological Research Letters*, 95:1381, 2024a. doi: 10.1785/0220240136.

Nye, T., Sahakian, V., and Melgar, D. Modeling ground motions and crustal deformation from tsunami earthquakes: Rupture parameter constraints from the 2010 Mentawai event. *Seismica*, 3(2), 2024b. doi: 10.26443/seismica.v3i2.1152.

Nye, T., Schlesinger, A., Sahakian, V., Melgar, D., Babaie Mahani, A., Williamson, A., Ferguson, E., Lux, A., and Pirenne, B. Cascadia subduction zone earthquake simulations for earthquake early warning testing, 2026. doi: 10.5683/SP3/CZECEG.

Parker, G., Stewart, J., Boore, D., Atkinson, G., and Hassani, B. *NGA-Subduction Global Ground-Motion Models with Regional Adjustment Factors*. 2020. doi: 10.55461/inke2546.

Poulos, A., Hirakawa, E., Parker, G. A., and Baltay, A. Orientation dependence of probabilistic seismic hazard estimates from CyberShake physics-based simulations. *Bulletin of the Seismological Society of America*, 2026. doi: 10.1785/0120250187.

Priest, G. R., Zhang, Y., Witter, R. C., Wang, K., Goldfinger, C., and Stimely, L. Tsunami impact to Washington and northern Oregon from segment ruptures on the southern Cascadia subduction zone. *Natural Hazards*, 72(2):849–870, 2014. doi: 10.1007/s11069-014-1041-7.

Pujades, L. G., Ugalde, U., Canas, J. A., Navarro, M., Badal, F., and Corchete, V. Intrinsic and scattering attenuation from observed seismic codas in the Almeria Basin (southeastern Iberian Peninsula. *Geophysical Journal International*, 129(2):281–291, 1997. doi: 10.1111/j.1365-246X.1997.tb01581.x.

Rodgers, A. J., Pitarka, A., and McCallen, D. B. The effect of fault geometry and minimum shear wavespeed on 3D ground-motion simulations for an Mw 6.5 Hayward Fault scenario earthquake, San Francisco Bay Area, Northern California. *Bulletin of the Seismological Society of America*, 109(4):1265–1281, 2019. doi: 10.1785/0120180290.

Rosenberger, A. Real-time ground-motion analysis: Distinguishing P and S arrivals in a noisy environment. *Bulletin of the Seismological Society of America*, 100(3):1252–1262, 2010. doi: 10.1785/0120090265.

Rosenberger, A. Three component accelerometer signal processing for WARN. Technical report, Zenodo, 2019. doi: 10.5281/ZENODO.4774354.

Rosenberger, A., Banville, S., Collins, P., Henton, J., and Ferguson, E. Kalman filter algorithm for the joint processing of GNSS PPP and accelerometer data, EEW parameters from the unbiased displacement time-series. Technical report, Zenodo, 2018. doi: 10.5281/ZENODO.4774348.

Rosenberger, A., Crosby, B., Ferguson, E., Heesemann, M., Leech, B., MacArthur, M., Schlesinger, A., Scholte, L., Wang, L., and Zheng, Y. Epicentre location and association of events from P-wave on-set times, magnitude estimation. Technical report, Zenodo, 2019a. doi: 10.5281/ZENODO.4774330.

Rosenberger, A., Ferguson, E., and Schlesinger, A. Testing the Associator: Simulating Seismic Events. Technical report, 2019b. doi: 10.5281/ZENODO.4815165.

Ross, Z. E. and Ben-Zion, Y. Automatic picking of direct P, S seismic phases and fault zone head waves. *Geophysical Journal International*, 199(1):368–381, 2014. doi: 10.1093/gji/ggu267.

Ross, Z. E., White, M. C., Vernon, F. L., and Ben-Zion, Y. An improved algorithm for real-time S wave picking with application to the (augmented) ANZA network in Southern California. *Bulletin of the Seismological Society of America*, 106(5):2013–2022, 2016. doi: 10.1785/0120150230.

Ruhl, C. J., Melgar, D., Grapenthin, R., and Allen, R. M. The value of real-time GNSS to earthquake early warning. *Geophysical Research Letters*, 44(16):8311–8319, 2017. doi: 10.1002/2017gl074502.

Ruhl, C. J., Melgar, D., Chung, A. I., Grapenthin, R., and Allen, R. M. Quantifying the value of real-time geodetic constraints for earthquake early earning using a global seismic and geodetic data set. *Journal of Geophysical Research: Solid Earth*, 124(4): 3819–3837, 2019. doi: 10.1029/2018jb016935.

Sahakian, V., Baltay, A., Hanks, T., Buehler, J., Vernon, F., Kilb, D., and Abrahamson, N. Decomposing leftovers: Event, path, and site residuals for a small-magnitude Anza region GMPE. *Bulletin of the Seismological Society of America*, 108(5A):2478–2492, 2018. doi: 10.1785/0120170376.

Satake, K., Wang, K., and Atwater, B. F. Fault slip and seismic moment of the 1700 Cascadia earthquake inferred from Japanese tsunami descriptions. *Journal of Geophysical Research: Solid Earth*, 108(B11), 2003. doi: 10.1029/2003jb002521.

Schlesinger, A., Kukovica, J., Rosenberger, A., Heesemann, M., Pirenne, B., Robinson, J., and Morley, M. An Earthquake Early Warning System for Southwestern British Columbia. *Frontiers in Earth Science*, 9, 2021. doi: 10.3389/feart.2021.684084.

Sheen, D., Park, J., Chi, H., Hwang, E., Lim, I., Seong, Y. J., and Pak, J. The First Stage of an Earthquake Early Warning System in South Korea. *Seismological Research Letters*, 88(6):1491–1498, 2017. doi: 10.1785/0220170062.

Small, D. T. and Melgar, D. Geodetic Coupling Models as Constraints on Stochastic Earthquake Ruptures: An Example Application to PTHA in Cascadia. *Journal of Geophysical Research: Solid Earth*, 126(7), 2021. doi: 10.1029/2020jb021149.

Small, D. T. and Melgar, D. Can Stochastic Slip Rupture Modeling Produce Realistic M9+ Events? *Journal of Geophysical Research: Solid Earth*, 128(3), 2023. doi: 10.1029/2022jb025716.

Smyth, A. and Wu, M. Multi-rate Kalman filtering for the data fusion of displacement and acceleration response measurements in dynamic system monitoring. *Mechanical Systems and Signal Processing*, 21(2):706–723, 2007. doi: 10.1016/j.ymssp.2006.03.005.

Suárez, G., Espinosa-Aranda, J. M., Cuéllar, A., Ibarrola, G., García, A., Zavala, M., Maldonado, S., and Islas, R. A Dedicated Seismic Early Warning Network: The Mexican Seismic Alert System (SASMEX). *Seismological Research Letters*, 89(2A):382–391, 2018. doi: 10.1785/0220170184.

Thakoor, K., Andrews, J., Hauksson, E., and Heaton, T. From earthquake source parameters to ground-motion warnings near you: The ShakeAlert earthquake information to ground-motion (eqInfo2GM) method. *Seismological Research Letters*, 90(3): 1243–1257, 2019. doi: 10.1785/0220180245.

Thompson, M., Renate Hartog, J., and Wirth, E. A. A population-based performance evaluation of the ShakeAlert earthquake early warning system for M 9 megathrust earthquakes in the Pacific Northwest, U.S.A. *Bulletin of the Seismological Society of America*, 114(2):1103–1123, 2023. doi: 10.1785/0120230055.

Tréhu, A. M., Braunmiller, J., and Davis, E. Seismicity of the Central Cascadia Continental Margin near 44.5° N: A decadal view. *Seismological Research Letters*, 86(3):819–829, 2015. doi: 10.1785/0220140207.

Trugman, D. T., Page, M. T., Minson, S. E., and Cochran, E. S. Peak Ground Displacement Saturates Exactly When Expected: Implications for Earthquake Early Warning. *Journal of Geophysical Research: Solid Earth*, 124(5):4642–4653, 2019. doi: 10.1029/2018jb017093.

Walton, M. A., Staisch, L. M., Dura, T., Pearl, J. K., Sherrod, B., Gomberg, J., Engelhart, S., Tréhu, A., Watt, J., Perkins, J., Witter, R. C., Bartlow, N., Goldfinger, C., Kelsey, H., Morey, A. E., Sahakian, V. J., Tobin, H., Wang, K., Wells, R., and Wirth, E. Toward an Integrative Geological and Geophysical View of Cascadia Subduction Zone Earthquakes. *Annual Review of Earth and Planetary Sciences*, 49(1):367–398, 2021. doi: 10.1146/annurev-earth-071620-065605.

Wang, K. and Tréhu, A. M. Invited review paper: Some outstanding issues in the study of great megathrust earthquakes—The Cascadia example. *Journal of Geodynamics*, 98:1–18, 2016. doi: 10.1016/j.jog.2016.03.010.

Wessel, P., Luis, J. F., Uieda, L., Scharroo, R., Wobbe, F., Smith, W. H. F., and Tian, D. The Generic Mapping Tools Version 6. *Geochemistry, Geophysics, Geosystems*, 20(11):5556–5564, 2019. doi: 10.1029/2019gc008515.

Williamson, A., Lux, A., and Allen, R. M. Improving magnitude estimates in the EPIC earthquake early warning algorithm. *Seismological Research Letters*, 97(1):233–245, 2026. doi: 10.1785/0220240453.

Wirth, E. A., Grant, A., Marafi, N. A., and Frankel, A. D. Ensemble ShakeMaps for Magnitude 9 Earthquakes on the Cascadia Subduction Zone. *Seismological Research Letters*, 92(1):199–211, 2020. doi: 10.1785/0220200240.

Wirth, E. A., Sahakian, V. J., Wallace, L. M., and Melnick, D. The occurrence and hazards of great subduction zone earthquakes. *Nature Reviews Earth & Environment*, 3(2):125–140, 2022. doi: 10.1038/s43017-021-00245-w.

Worden, C. B., Gerstenberger, M. C., Rhoades, D. A., and Wald, D. J. Probabilistic Relationships between Ground-Motion Parameters and Modified Mercalli Intensity in California. *Bulletin of the Seismological Society of America*, 102(1):204–221, 2012. doi: 10.1785/0120110156.

Wu, Y. and Zhao, L. Magnitude estimation using the first three seconds P-wave amplitude in earthquake early warning. *Geophysical Research Letters*, 33(16), 2006. doi: 10.1029/2006gl026871.

Wu, Y.-M., Mittal, H., Chen, D.-Y., Hsu, T.-Y., and Lin, P.-Y. Earthquake Early Warning Systems in Taiwan: Current Status. *Journal of the Geological Society of India*, 97(12):1525–1532, 2021. doi: 10.1007/s12594-021-1909-6.

Wurman, G., Allen, R. M., and Lombard, P. Toward earthquake early warning in northern California. *Journal of Geophysical Research: Solid Earth*, 112(B8), 2007. doi: 10.1029/2006jb004830.

Zhang, G.-q., Li, D.-n., Gao, Y., and Yang, J.-q. A Magnitude Estimation Approach and Application to the Yunnan Earthquake Early Warning Network. *Seismological Research Letters*, 94(1): 234–242, 2022. doi: 10.1785/0220220093.

Zhang, H., Jin, X., Wei, Y., Li, J., Kang, L., Wang, S., Huang, L., and Yu, P. An Earthquake Early Warning System in Fujian, China. *Bulletin of the Seismological Society of America*, 106(2):755–765, 2016. doi: 10.1785/0120150143.

Zhu, L. and Rivera, L. A. A note on the dynamic and static displacements from a point source in multilayered media. *Geophysical Journal International*, 148(3):619–627, 2002. doi: 10.1046/j.1365-246x.2002.01610.x.

Ziv, A., Eisermann, A. S., Volk, O., and Zbeda, I. Introducing ViDA3, an earthquake early warning algorithm for offshore hypocenter determination using onshore seismic networks. *Bulletin of the Seismological Society of America*, 114(5):2446–2456, 2024. doi: 10.1785/0120230302.

Zollo, A., Iannaccone, G., Lancieri, M., Cantore, L., Convertito, V., Emolo, A., Festa, G., Gallovič, F., Vassallo, M., Martino, C., Satriano, C., and Gasparini, P. Earthquake early warning system in southern Italy: Methodologies and performance evaluation. *Geophysical Research Letters*, 36(5), 2009. doi: 10.1029/2008gl036689.